



Amorphization driven Na-Alloying in SixGe_{1-x} alloy nanowires for Na-ion batteries

Syed Abdul Ahad, Seamus Kilian, Maria Zubair, VASILY LEBEDEV, Karrina McNamara, KEVIN M. RYAN, TADHG KENNEDY, HUGH GEANEY

Publication date

06-08-2021

Published in

Journal of Materials Chemistry A, 36, pp. 20626-20634

Licence

This work is made available under the [CC BY-NC-SA 4.0](#) licence and should only be used in accordance with that licence. For more information on the specific terms, consult the repository record for this item.

Document Version

1

Citation for this work (HarvardUL)

Abdul Ahad, S., Kilian, S., Zubair, M., LEBEDEV, V., McNamara, K., RYAN, K.M., KENNEDY, T. and GEANEY, H. (2021) 'Amorphization driven Na-Alloying in SixGe_{1-x} alloy nanowires for Na-ion batteries', available: <https://doi.org/10.34961/researchrepository-ul.22274752.v1>.

This work was downloaded from the University of Limerick research repository.

For more information on this work, the University of Limerick research repository or to report an issue, you can contact the repository administrators at ir@ul.ie. If you feel that this work breaches copyright, please provide details and we will remove access to the work immediately while we investigate your claim.

Amorphization driven Na-Alloying in $\text{Si}_x\text{Ge}_{1-x}$ alloy nanowires for Na-ion batteries

Syed Abdul Ahad, Seamus Kilian, Maria Zubair, Vasily A. Lebedev, Karrina McNamara, Kevin M. Ryan, Tadhg Kennedy and Hugh Geaney*

*Department of Chemical Sciences and Bernal Institute, University of Limerick, Limerick V94 T9PX, Ireland. E-mail: Hugh.Geaney@ul.ie

Abstract

Here we report the use of 1D $\text{Si}_x\text{Ge}_{1-x}$ ($x = 0.25, 0.5, 0.75$) alloy nanowires (NWs) as anode materials for Na-ion batteries (NIB). The strategy involves the synthesis of crystalline $\text{Si}_x\text{Ge}_{1-x}$ NWs via the solution-liquid solid (SLS) mechanism, followed by amorphization to activate the material for Na-ion cycling within an NIB. This study demonstrates the successful activation of $\text{Si}_x\text{Ge}_{1-x}$ amorphous NW alloys, with a- $\text{Si}_{0.5}\text{Ge}_{0.5}$ delivering 250 mAh g^{-1} as compared to a-Ge NWs delivering only 107 mAh g^{-1} after 100 cycles. Also, amorphization proved to be a critical step, since crystalline NWs failed to activate in NIB. However, Si NWs performed poorly during Na-ion cycling even after amorphization, with this behaviour explained by poor comparative Na-ion diffusivity. Further investigations on the impact of the relative content of Ge within the amorphized $\text{Si}_x\text{Ge}_{1-x}$ NWs, Na-ion diffusivity and electrode degradation during cycling were also performed. Notably, the incorporation of Ge in a- $\text{Si}_x\text{Ge}_{1-x}$ alloy boosted Na ion diffusivity in amorphized alloy, resulting in improved cyclic performance and rate capability as compared to parent a-Si and a-Ge NWs.

Introduction

The revolution in the fields of portable devices, electric vehicles and stationary grid systems has put significant pressure on the development of rechargeable batteries. Among rechargeable chemistries, LIBs have held a dominant position across these various sectors. However, diminishing Li reserves and need to reduce the use of toxic elements (e.g. Cobalt) in energy storage applications, has led to interest in alternate metal-ion chemistries such as sodium (Na) and potassium (K) - ion batteries. NIBs are particularly of interest due to the abundant resources of Na salts and price competitiveness when compared to LIBs.¹⁻⁴

In comparison to Li-ions, Na-ions are larger in size (1.02 Å vs. 0.76 Å), with only slightly higher redox potential (-2.71 V vs. -3.02 V against standard hydrogen electrode (SHE)).⁵ Although the theoretical capacity of Na metal is 1165 mAh g⁻¹, the use of Na metal as an anode is limited due to safety concerns caused by dendrite formation during cycling and subsequent short circuits; problems shared by Li-metal anodes.⁵⁻⁷ Therefore, there is a need to develop alternate anode systems for safe operation and subsequent commercialization of NIBs. Graphite is naturally a material of interest since it provides a stable specific capacity of 372 mAh g⁻¹ in LIBs. However, the sluggish diffusion of Na-ion in graphite leads to poor activation,⁸ therefore alternate anode materials such as hard carbon, conversion and alloying mode materials with higher deliverable specific capacities in NIBs are being investigated.⁹⁻¹¹ Among alloying mode materials such as Si, Ge and Sn which have delivered high specific capacities in LIBs have also been tested as anode materials in NIBs.¹²⁻¹⁴ These materials have high theoretical capacities of 957 mAh g⁻¹ (Si), 369 mAh g⁻¹ (Ge) and 847 mAh g⁻¹ (Sn) based on the formation of NaSi, NaGe and Na_{3.75}Sn in the fully sodiated states; with respective volume expansions of 114 %, 225 % and 420 %.¹⁵

While crystalline Si (c-Si) and Ge (c-Ge) have high deliverable specific capacities of ~ 2500 mAh g⁻¹ and ~ 1000 mAh g⁻¹ in LIBs due to their high Li-ion diffusivity,^{16–21} these materials struggle to activate in their crystalline form in NIBs, due to prohibitive Na-ion diffusivity.^{22,23} Strategies to overcome this issue typically involve the use of alloying material in an amorphous state, since theoretical calculations suggest that the diffusion barrier for Na insertion significantly decreases in an amorphous state compared to their crystalline counterpart.^{24,25} One such example is that of Si, which has been shown to activate in NIBs if it is amorphous and has nanoscale features.^{26,27} Despite this, the ability of a-Si to activate even in its amorphous state has proven challenging, with several reports suggesting achievable specific capacities of just 200 – 300 mAh g⁻¹ using composite slurries.^{28–30} These values are significantly lower than the theoretical capacity of a-Si at a fully sodiated state of Na_{0.76}Si, which is expected to deliver 725 mAh g⁻¹.²⁷ On the other hand, a-Ge thin films and Ge NWs have demonstrated activity in NIBs after being amorphized during preconditioning lithiation/delithiation steps.^{25,31,32} Another strategy to overcome the Na ion diffusion barrier is through alloying of different Na active materials to mitigate the poor activation of parent Si and Ge. Various binary and ternary alloy compositions containing either Si or Ge such as Sb-Si,³³ Sn-Si,³⁴ Sn-Ge³⁵ and Sn-Ge-Sb³⁶ have been tested in NIBs. However, to the best of our knowledge, there have been no reports where the behaviour of Si and Ge as binary Si-Ge alloys have been explored in NIBs, despite their highly impressive performance in LIBs and potential for compositional tuneability.^{37–39}

In this work we explore the use of Si_xGe_{1-x} ($x = 0.25, 0.5, 0.75$) in NIBs and study the impact of introducing these elements together as alloys in determining the electrochemical performance and Na-ion diffusivity. The growth of binder-free NWs on current collectors allowed an examination of the role of Si and Ge alloy composition on the electrochemical performance, without any influence of binder and carbon additives. The study shows that unlike crystalline forms of Si, Si_xGe_{1-x} and Ge, the amorphized form of NWs successfully activate in

NIBs. The role of Ge incorporation on Na-ion diffusion and on cycling performance of amorphized $\text{Si}_x\text{Ge}_{1-x}$ NWs is also discussed. We finally demonstrate that certain $\text{a-Si}_x\text{Ge}_{1-x}$ alloy compositions (i.e. $\text{a-Si}_{0.5}\text{Ge}_{0.5}$ and $\text{a-Si}_{0.25}\text{Ge}_{0.75}$) outperform pure a-Si and a-Ge during electrochemical cycling.

Experimental Section

Material synthesis: There The NWs were grown on a SS foil (Pi-Kem UK) with a thickness of 0.1 mm. A 20 nm Tin (Sn, 99.999 % - Kurt. J. Lesker) seed layer was thermally evaporated on the roughened SS substrates and stored in a glove box to avoid any oxidation prior to NW synthesis.³⁹ The NW synthesis reaction was conducted in a 3-zone furnace using a round bottom flask attached to a water condenser. The long-neck round bottom flask containing 8 ml squalane with Sn-coated SS substrates immersed in it and placed in the furnace. Once sealed, the reaction temperature was ramped up to 145 oC and a vacuum of 100 mTorr was applied for 1 hr to remove any moisture from the system. Afterwards, the temperature was ramped to 460 °C under Ar gas with a water condenser attached to control the reflux during the reaction. For Si, 1 ml of Phenylsilane (PS, 97 %) was injected via the septum cap and the reaction was allowed to proceed for 2 hrs. For $\text{Si}_x\text{Ge}_{1-x}$, a mixture of Triphenylgermane - TPG: Squalane (1:4) and a fixed amount of 0.7 ml PS was injected in the reaction setup and allowed to react for 1 hr. The TPG: Squalane (1:4) volume was varied between 30 – 400 μl to obtain various compositions of $\text{Si}_x\text{Ge}_{1-x}$ NWs. For Ge NWs, 0.25 ml of Diphenyl germane (DPG) was injected and allowed to react for 25 mins. The reactions were terminated by opening the furnace and allowing it to cool down. The substrates were later extracted, washed with toluene and dried in air. The NW loading varied from 0.13 - 0.19 mg cm^{-2} .

Material characterization: The weight of the samples were measured using a Sartorius Ultra-Microbalance (SE2, repeatability $\pm 0.25 \mu\text{g}$). X-ray diffraction (XRD) analysis was performed

using PANalytical Empyrean instrument fitted with Cu K α source ($\lambda = 1.5418 \text{ \AA}$) and an X'celerator detector. Scanning electron microscopy (SEM) and Electron dispersive spectroscopy (EDS) analysis was performed on a Hitachi SU-70 operated at 20 kV. The EDS analysis was performed at various parts of the substrate to ascertain the Si/Ge alloy ratios of the NWs. TEM analysis was performed using a JEOL (JEM – 2100F) operated at 200 kV, fitted with a Genesis EDAX detector. For ex-situ SEM and TEM analysis, the electrodes were extracted in the delithiated and desodiated state and washed with acetonitrile, 1mM acetic acid, distilled water and ethanol in that sequence to remove any SEI layer before further analysis. The Raman spectroscopy was performed using a Horiba Labram 300 spectrometer fitted with a 532 nm laser. The X-ray photoelectron spectroscopy (XPS) was carried out using a Kratos AXIS ULTRA spectrometer fitted with a mono Al K α (1486.58 eV) X-ray gun. Calibration was performed using C 1s line at 284.8 eV while construction and peak fitting was performed using CasaXPS software. The XPS samples were briefly washed with Diethyl carbonate - DEC (for LIB) and Dimethyl ether - DME (for NIB) to remove any excess electrolyte before carefully transferring to the XPS chamber to minimize any air exposure and subsequent oxidation of SEI species.

Electrochemical characterization: The electrochemical characterization was performed by assembling cells in an argon filled glove box (Vigor) using Swagelok cells (for all prelithiation experiments) or coin cells (CR 2032, for all NIB cycling). For prelithiation, Swagelok configuration was used where NWs grown on SS foil were used as working electrode while Li metal was used as counter electrode. The electrolyte and separator were 1 M LiPF₆ (EC: DEC) + 3% VC (Sigma Aldrich) and Celgard respectively. For NIB testing, the delithiated (and thus amorphized) electrodes were extracted from Swagelok cells, briefly washed with DEC, dried and re-assembled in a coin cell with sodium metal as counter electrode. The electrolyte and separator used for NIB testing was 1 M NaOTf (Solvionic) in DEGDME and glass fiber (GF/D,

Whatman®) as the electrolyte and separator respectively. Galvanostatic cycling was carried out using a biologic MPG-2 instrument in a potential range of 0.005 – 2.0 V. All current densities were calculated based on the mass of all active components. Cyclic voltammetry (CV) was carried out using a 0.02 mV/s scan rate while electrochemical impedance spectroscopy (EIS) was carried out between a frequency range of 0.1 Hz – 10 kHz.

Results and Discussion

The scheme for the formation of Si, Ge and $\text{Si}_x\text{Ge}_{1-x}$ NWs for NIBs is illustrated in **Figure 1a**. The NWs were prepared using a solution-liquid-solid (SLS) technique using Sn as a seed to grow NWs.³⁹ The injection of different precursors (Phenylsilane - PS, Triphenyl germane - TPG and Diphenyl germane - DPG) in a high boiling point solvent (HBS) resulted in the growth of Sn-seeded Si, $\text{Si}_x\text{Ge}_{1-x}$ ($x = 0.25, 0.5, 0.75$) and Ge NWs. The alloy $\text{Si}_x\text{Ge}_{1-x}$ NWs were prepared by injecting a mixture of TPG and PS, with the composition tuned by the volumes of the precursors added. The scanning electron microscopy (SEM) images of Si, $\text{Si}_{0.5}\text{Ge}_{0.5}$ and Ge NWs revealed dense NW growth on stainless steel (SS) substrate (**Figure 1b-d**). The several micron long NWs have diameters ranging from 40 nm to 200 nm with an average diameter of 105.8 nm, 94.8 nm and 96.8 nm for Si, $\text{Si}_{0.5}\text{Ge}_{0.5}$ and Ge respectively (**Figure S1**). The energy-dispersive X-ray spectroscopy (EDS) analysis of different alloy compositions revealed that the Sn content in the final composition is low and ranges from 4-6 at. % only. Therefore, for simplicity, all the alloys mentioned in this study were based on the nominal compositions of just Si and Ge atomic ratios (**Figure S2**). The transmission electron microscope (TEM) image presented in **Figure 2a** shows a low-res image of one of the alloy composition i.e. $\text{Si}_{0.5}\text{Ge}_{0.5}$ alloy NW, with a typical diameter of 95.1 nm. The HRTEM image presented in **Figure 2b** was examined using a fast Fourier transform (FFT), and the calculated pattern was indexed with respect to the Fd3m space group of Si and Ge. The corresponding (111), (002) and (220) planes

are shown on the HRTEM image of the $\text{Si}_{0.5}\text{Ge}_{0.5}$ NW (**Figure 2b - inset**). The scanning transmission electron microscopy (STEM) analysis further confirmed the homogeneous distribution of Si and Ge in the $\text{Si}_{0.5}\text{Ge}_{0.5}$ alloy NW with sparse distribution of Sn in the nanowire (**Figure 2c**). Sn signals in the NW might be due to the metal incorporation at twin defect sites commonly reported in earlier studies as well.^{39,40}

The X-ray diffraction (XRD) data presented in **Figure 2d** confirmed the presence of a prominent (111) peak for the pure Si and Ge NWs present at 28.3° and 27.2° respectively. Meanwhile the (111) reflection from $\text{Si}_{0.5}\text{Ge}_{0.5}$ lies between that of Si and Ge, with no additional peak visible from either parent Si or Ge phase; suggesting pure phase formation of $\text{Si}_{0.5}\text{Ge}_{0.5}$. A comparison of XRD spectra of all the synthesized alloy NWs suggested that from Si-rich $\text{Si}_{0.75}\text{Ge}_{0.25}$ towards Ge-rich $\text{Si}_{0.25}\text{Ge}_{0.75}$, the (111) peak shifted from high-angle parent Si phase towards low angle parent Ge phase (**Figure S3a**).^{38,39} The Raman spectra shown in **Figure 2e** further confirmed the successful formation of $\text{Si}_{0.5}\text{Ge}_{0.5}$ alloy when an additional

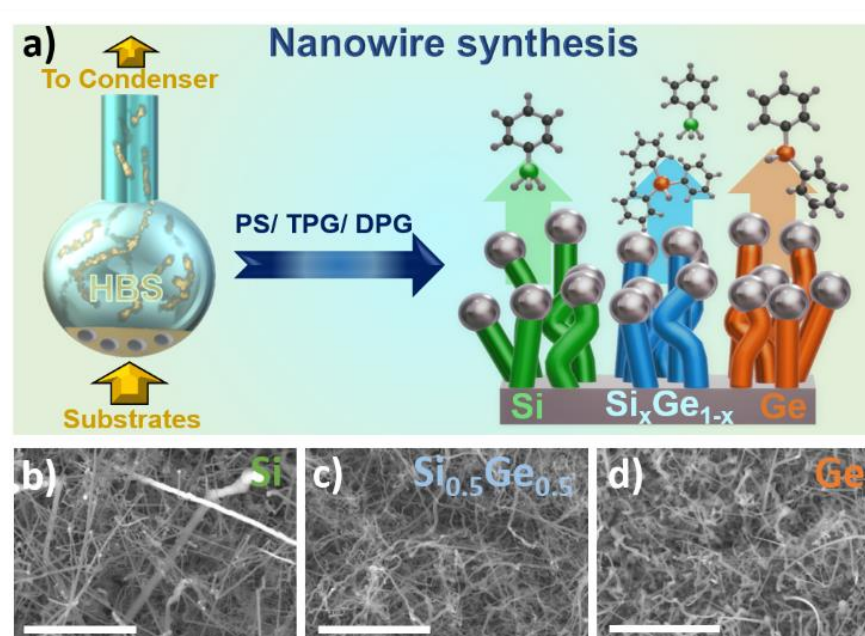


Figure 1 Schematic illustration of the synthesis process of Si, $\text{Si}_x\text{Ge}_{1-x}$ and Ge NWs. SEM image of Sn-seeded (b) Si NWs, (c) $\text{Si}_{0.5}\text{Ge}_{0.5}$ NWs and (d) Ge NWs. All scale bars are equal to 5 μm .

peak appeared around 400 cm^{-1} , characteristic of Si-Ge bond, in addition to that of Si-Si (490 cm^{-1}) and Ge-Ge (300 cm^{-1}) bond. With increasing Ge content, the Si-Si bond peak shifted towards a lower wavenumber while the Ge-Ge shifted towards a higher wavenumber due to the strain induced in the formed alloys (**Figure S3b**). The decrease in relative peak intensity of Si-Si and Si-Ge peak intensity was caused by an increase in Ge atoms per Si atom in the alloy structure, which ultimately reduced the mean frequency of the Si-Si and Si-Ge active modes.^{38,41}

X-ray photoelectron spectroscopy (XPS) analysis was performed to determine the chemical moieties present in $\text{Si}_{0.5}\text{Ge}_{0.5}$ alloy. The core-level spectra of various elements present in $\text{Si}_{0.5}\text{Ge}_{0.5}$ alloy is shown in **Figure 2f-h**. For Ge, the deconvoluted peaks at 29.32 eV and 29.90 eV were assigned to Ge and Si-Ge simultaneously, due to XPS limitations in detecting small binding energy difference between Ge-Ge and Si-Ge bonds.⁴¹ The peaks at 30.13 eV and 32.58 eV were associated with GeO and GeO_2 present on the surface (**Figure 2f**). Similarly for Si, the deconvoluted peaks at 99.43 eV and 100.06 eV can be ascribed to Si and Si-Ge alloy while other species present were $\text{Si}_x\text{-C}_x$, Si_xO_y and SiO_x surface oxide layers, typically formed in this type of fabrication process of NWs (**Figure 2g**).⁴²⁻⁴⁴ The Sn spectra also revealed the presence of Sn, SnO and SnO_2 peaks at 485.11 eV, 485.8 eV and 487.32 eV respectively (**Figure 2h**). The corresponding core-level spectra for C and O is given in **Figure S4**. The carbon decomposition products are possibly coming from decomposition of squalane, PS and TPG during the synthesis process. While the air exposure post synthesis, forms a thin metal (Sn, Si, Ge) – oxide layer on NWs.^{44,45}

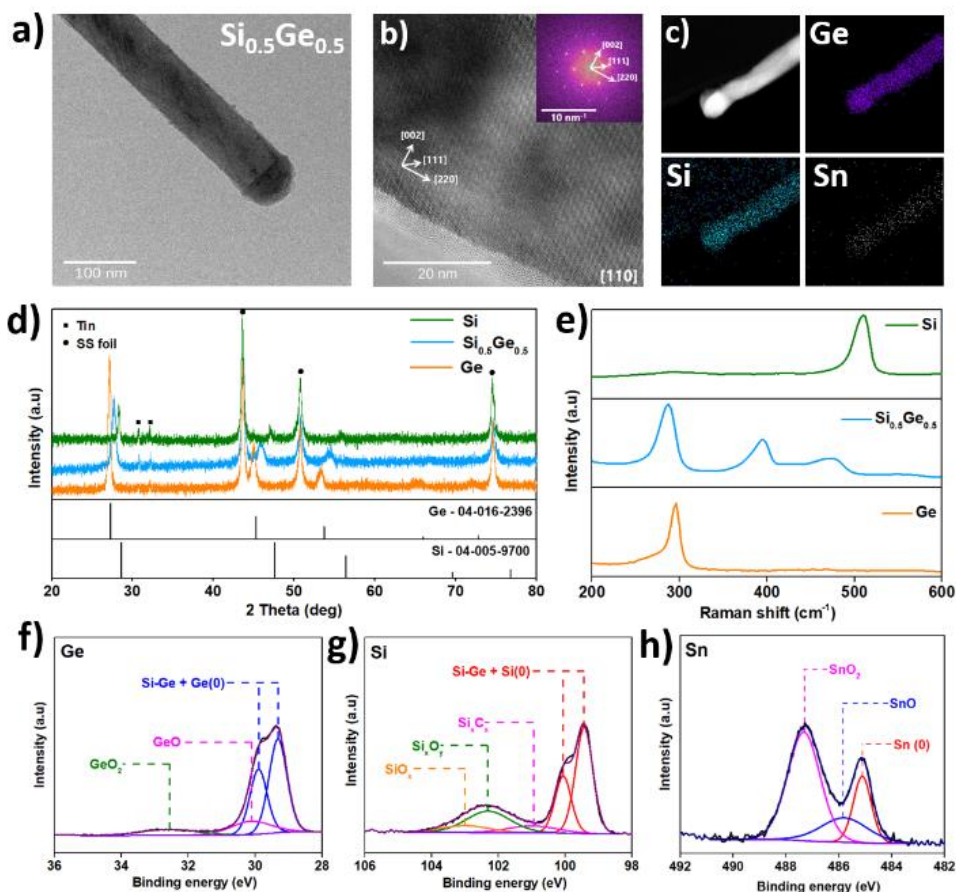


Figure 2 (a) TEM image, (b) HRTEM image with FFT (inset), (c) STEM and corresponding EDX mapping of Si, Ge and Sn elemental distribution in $\text{Si}_{0.5}\text{Ge}_{0.5}$ NW. (d) XRD analysis of Si, $\text{Si}_{0.5}\text{Ge}_{0.5}$ and Ge NW between 10° and 80° with corresponding standard patterns of pure Si and pure Ge phases. (e) Raman spectra of Si, $\text{Si}_{0.5}\text{Ge}_{0.5}$ and Ge NWs obtained using green laser light. XPS analysis of $\text{Si}_{0.5}\text{Ge}_{0.5}$ NWs representing core-level spectra of (f) Ge, (g) Si and (h) Sn.

To amorphize the c-NWs, the electrodes were cycled between a voltage range of 0.005 V – 2.0 V at a rate of C/5 in a Li half-cell (**Figure S5a**). To compare the lithiation/delithiation potential changes of parent phases vs. alloy NWs, differential capacity plots are presented in **Figure 3a-c**. These plots clearly illustrate the 1st lithiation peak at 0.088 V, 0.201 V and 0.324 V for Si, $\text{Si}_{0.5}\text{Ge}_{0.5}$ and Ge respectively. Two major delithiation peaks were noted at 0.309 V and 0.460 V for Si, with a single prominent peak at 0.495 V and 0.510 V for $\text{Si}_{0.5}\text{Ge}_{0.5}$ and Ge respectively. No apparent lithiation/de-lithiation peaks were observed in $\text{Si}_{0.5}\text{Ge}_{0.5}$ from the parent Si and Ge phase which is consistent with a lack of phase segregation in the subsequent electrochemical cycles (**Figure 3a-c**).^{39,46,47} In addition, no apparent peaks from Sn were

observed, suggesting that any Sn lithiation-delithiation peaks may be been masked due to the high peak currents originating from the primary Si/Ge electrochemical processes. The corresponding voltage-capacity plots for 10 cycles confirmed the reversible lithiation/delithiation mechanism in the parent phases as well as the alloy NWs (**Figure S5b-d**). A comparison of specific capacities of parent Si, Ge and $\text{Si}_x\text{Ge}_{1-x}$ alloys is discussed in **Figure S6**. For clear distinction from crystalline NWs, henceforth, the amorphized electrodes will be referred to as a-X ($X = \text{Si}, \text{Si}_x\text{Ge}_{1-x}, \text{Ge}$) in the text. The cycled NWs showed significant structural changes as compared to the original NW morphology (**Figure 3d-f**). Post cycling, a-Si, a- $\text{Si}_{0.5}\text{Ge}_{0.5}$ and a-Ge displayed mesh-like structure while still maintaining the overall outline of a 1D NW morphology. The DF-STEM and the corresponding EDS mapping of a- $\text{Si}_{0.5}\text{Ge}_{0.5}$ NW confirmed elemental homogeneity of Si and Ge throughout the NW along with sparse distribution of Sn (**Figure S7**). Unlike a-Si and a- $\text{Si}_{0.5}\text{Ge}_{0.5}$, the a-Ge NW additionally developed nanopores, caused by the electrochemical lithiation/delithiation process, which is typically reported in Ge NWs anodes cycled in LIBs (**Figure S8**).^{47,48} Other than the structural transformation, the presence of diffuse rings in the Electron diffraction (ED) pattern (shown as insets) indicate the transformation from crystalline to amorphous structure after electrochemical lithiation/delithiation cycles.^{37,49,50}

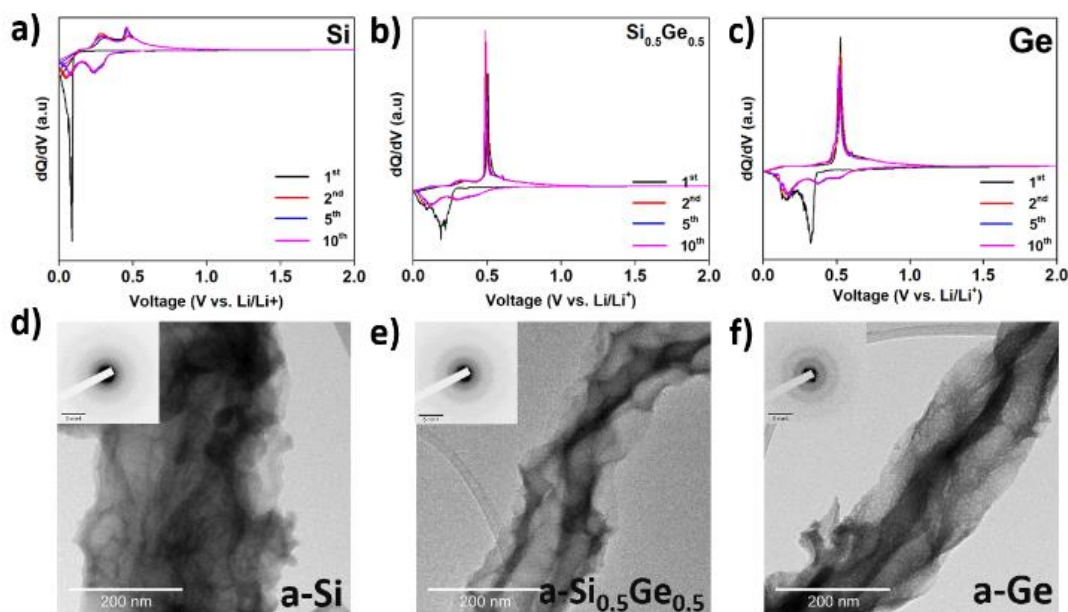


Figure 3 Differential capacity plots of (a) Si , (b) $\text{Si}_{0.5}\text{Ge}_{0.5}$ and (c) Ge NWs cycled in LIB between 0.005 - 2.0 V. TEM images of cycled (d) a-Si NWs, (e) a- $\text{Si}_{0.5}\text{Ge}_{0.5}$ NWs, and (f) a-Ge NWs in de-lithiated state with diffraction patterns shown as insets confirming amorphous phase of the cycled NWs. The scale bars in ED patterns (inset) correspond to 5 nm^{-1} .

The delithiated a-NWs extracted from Li-half cells were briefly washed with diethylene carbonate (DEC) before assembling in a Na-half cell. As illustrated in **Figure 4a**, the meshed NW take up Na ions during the sodiation process, with Na ion removal occurring during the de-sodiation process, generating a reversible electrochemical cycling process. The a-Si, a-Ge and a- $\text{Si}_x\text{Ge}_{1-x}$ NWs were cycled between 0.005 V – 2.0 V at a current density of 50 mA g^{-1} (**Figure 4b**). The galvanostatic cycling showed that a-Si, a- $\text{Si}_{0.5}\text{Ge}_{0.5}$ and a-Ge NWs delivered first cycle sodiation capacities of 257.1 mAh g^{-1} , 333.4 mAh g^{-1} and 538.7 mAh g^{-1} , with coulombic efficiencies of 11.5 % , 61.7 % and 71.8 % respectively. As compared to a- $\text{Si}_{0.5}\text{Ge}_{0.5}$ and a-Ge, the extremely low coulombic efficiency of the a-Si NWs first cycle suggests that the a-Si NWs did not cycle well, since the theoretical sodiation capacity of the a-Si is nearly 725 mAh g^{-1} .²⁷

The sodiation capacity of a-Si and a-Ge quickly fell to 10.4 mAh g⁻¹ and 230 mAh g⁻¹ after 50 cycles respectively, while a-Si_{0.5}Ge_{0.5} still maintained a high capacity of 305 mAh g⁻¹, with a capacity retention of 91.5 %. Based on the weight ratios of Si, Ge and Sn in a-Si_{0.5}Ge_{0.5} (**Figure S2**), each element delivered a capacity share of 77.7, 194.7 and 32.6 mAh g⁻¹ out of a total of 305 mAh g⁻¹. This suggests that the incorporation of Ge in the Si_xGe_{1-x} alloy helped in the activation of Si in alloy structure. The capacity share calculated for each element is based on the assumption that binary phases of sodiated Na_xSi, Na_xGe and Na_ySn will form at the fully sodiated state as previously reported.³⁴ Therefore, the maximum capacity share can be estimated based on the weight ratios of the elements present in the a-Si_{0.5}Ge_{0.5} alloy. After 100 cycles, the a-Si sodiation capacity dropped to a mere 10.1 mAh g⁻¹, with a capacity retention of just 3.93 %. In comparison, a-Si_{0.5}Ge_{0.5} and a-Ge exhibited specific capacities of 250.1 mAh g⁻¹ and 107 mAh g⁻¹, with capacity retentions of 75.1 % and 19.8 % respectively. A complete comparison of all the amorphous alloy NW compositions showed that with increasing Ge content in the alloy, the initial sodiation capacity increased but the capacity retention decreased significantly (**Figure S9a**). Among all the compositions tested, a-Si_{0.5}Ge_{0.5} had the highest capacity retention of 75 % after 100 cycles (**Figure S9b**). In strong contrast to the performance of the a-NWs, the crystalline Si_xGe_{1-x} alloy, parent Si and Ge NWs, delivered specific capacity values of not more than 10 mAh g⁻¹ after 50 cycles, proving that amorphization of the NWs is a critical step to activate sodiation processes (**Figure S10**).

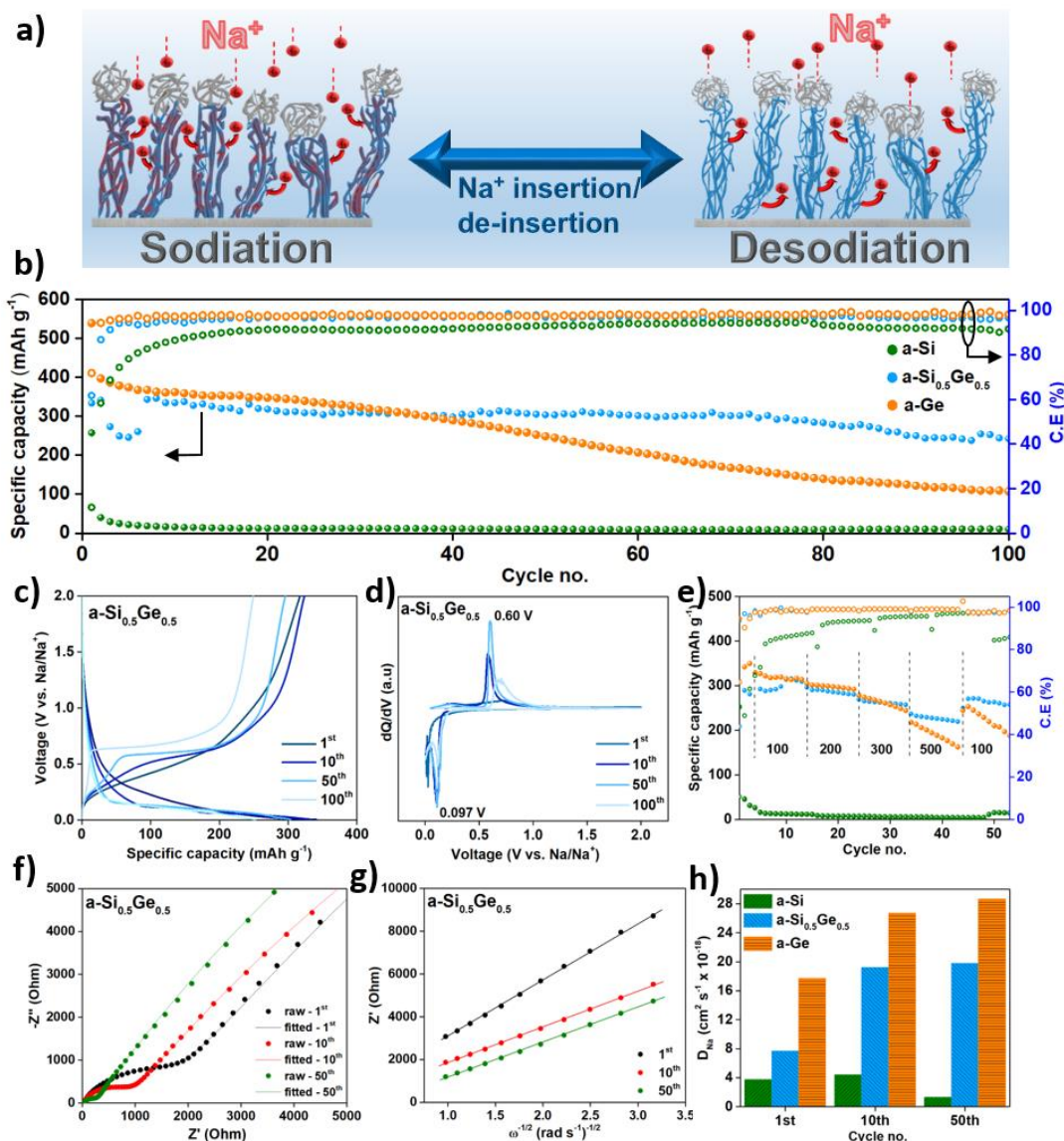


Figure 4 (a) Schematic illustration of sodiation, de-sodiation of meshed NWs in a NIB. (b) Specific capacity vs. cycle no. of a-Si, a-Si_{0.5}Ge_{0.5} and a-Ge NWs cycled between 0.005-2.0 V at 50 mA g⁻¹ in a NIB. (c) Voltage – capacity profile and (d) corresponding differential-capacity plot of a-Si_{0.5}Ge_{0.5} alloy NWs. (e) Rate capability testing of a-Si, a-Si_{0.5}Ge_{0.5} and a-Ge at different current densities of 100, 200, 300 and 500 mA g⁻¹. The first 3 cycles were performed at 50 mA g⁻¹ before switching to 100 mA g⁻¹ for rate-capability test. (f) Nyquist plot and (g) Z vs. $\omega^{-1/2}$ of a-Si_{0.5}Ge_{0.5} derived from Nyquist plot of a-Si_{0.5}Ge_{0.5}. (h) Comparison of apparent Na-ion diffusion coefficient of a-Si, a-Si_{0.5}Ge_{0.5} and a-Ge after various cycles.

The voltage-capacity profile of a-Si_{0.5}Ge_{0.5} and a-Ge revealed a single-step phase transformation from amorphous Ge / Si_{0.5}Ge_{0.5} phase to Na_xGe (Na_xSi_{0.5}Ge_{0.5}) phase during sodiation/desodiation process (**Figure 4c, S11a**). The a-Ge voltage-capacity profile also

showed large overpotentials (ΔE) as compared to a-Si_{0.5}Ge_{0.5} profile during cycling, which was clearly visible after 100 cycles. Further analysis of differential capacity plots confirmed sodiation of a-Si_{0.5}Ge_{0.5} and a-Ge at 0.097 V and 0.12 V, while desodiation occurred at 0.60 V and 0.63 V respectively (**Figure 4d, S11b**). Additionally, a broad shoulder peak appeared around 0.26 V during desodiation of a-Si_{0.5}Ge_{0.5} which could be ascribed to the desodiation of Na_xSn or Na_xSi (**Figure 4d**).^{34,51} However, no other sodiation/desodiation peaks from Sn were observed in any of the a-NW tested in this study, which signifies that the broad peak appearing around 0.26 V in a-Si_{0.5}Ge_{0.5} is from a-Si activation in the alloy NW.^{27,52} The parent a-Si NWs however, did not reveal any significant desodiation behaviour after the 1st sodiation half-cycle which suggests just the formation of SEI and irreversible sodium intercalation, as evident in voltage-capacity and differential capacity plot of a-Si (**Figure S11c, d**). The cyclic voltammetry (CV) analysis of a-Si, a-Si_{0.5}Ge_{0.5} and a-Ge revealed similar information and is presented in **Figure S12**. The rate capability analysed at different current densities demonstrates the robustness of a-Si_{0.5}Ge_{0.5} alloy in comparison to a-Ge and a-Si; especially evident at higher current densities. The a-Si_{0.5}Ge_{0.5} NWs delivered a capacity of 295.2 mAh g⁻¹, 292.10 mAh g⁻¹, 267.9 mAh g⁻¹ and 237.3 mAh g⁻¹ at 100 mA g⁻¹, 200 mA g⁻¹, 300 mA g⁻¹ and 500 mA g⁻¹ respectively (**Figure 4e**). The a-Ge however, could not retain higher capacities at high current densities of 300 mA g⁻¹ and 500 mA g⁻¹ and did not recover capacity once the current density was returned back to 100 mA g⁻¹, in contrast to a-Si_{0.5}Ge_{0.5}. As expected, a-Si maintained extremely low capacities (~ 10 mAh g⁻¹) throughout the different current densities tested. The rate capability test therefore suggests enhanced reversible electrochemical activity of the a-Si_{0.5}Ge_{0.5} NWs in comparison to the parent amorphous phases (Si, Ge) tested. Finally, a-Si_{0.5}Ge_{0.5} demonstrated relatively stable cyclic performance at 200 mA g⁻¹ with a specific capacity of 200 mAh g⁻¹, in comparison to a-Ge which failed post 100 cycles (**Figure S13**).

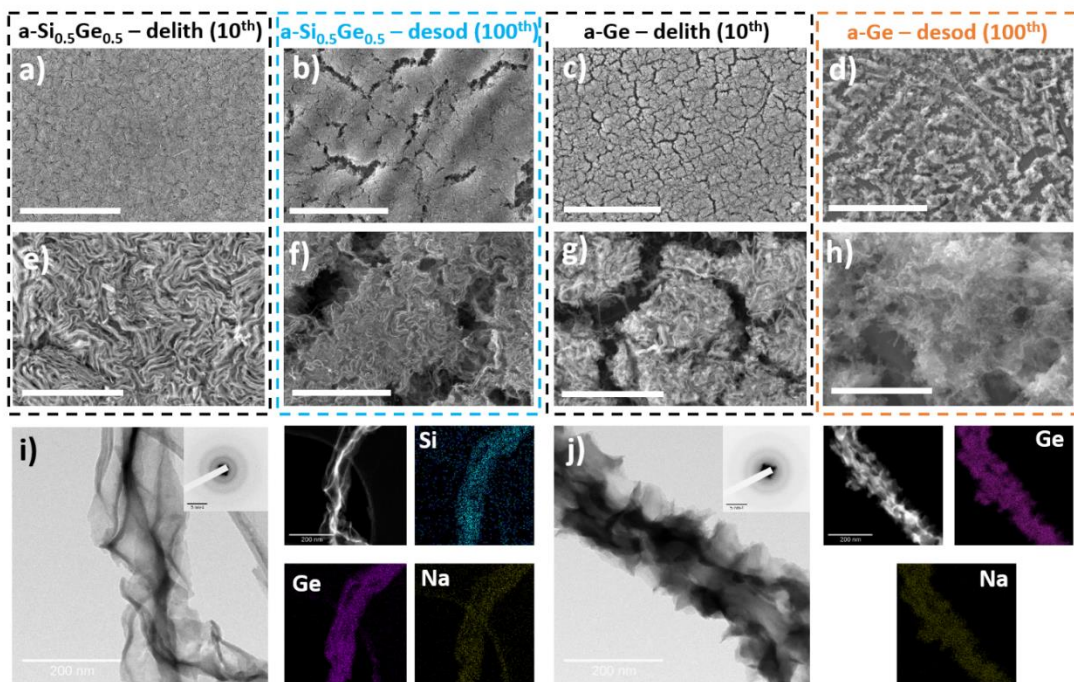


Figure 5 SEM image of (a, e) a-Si_{0.5}Ge_{0.5} – delithiated state after 10th cycle, (b, f) a-Si_{0.5}Ge_{0.5} – desodiated state after 100th cycle, (c, g) a-Ge – delithiated state after 10th cycle (d, h) a-Ge – desodiated state after 100th cycle. The scale bars in a, b, c & d image represents 50 μm while scale bar in e, f, g & h represents 5 μm . (i) TEM image with diffraction pattern (inset), STEM and elemental mapping of Si, Ge and Na of a-Si_{0.5}Ge_{0.5} in desodiated state after 100th cycle. (j) TEM image with diffraction pattern (inset), STEM and elemental mapping of Si, Ge and Na of a-Ge in desodiated state after 100th cycle. The scale bars in ED patterns (inset) correspond to 5 nm^{-1} .

To gain insight into the reaction kinetics of different materials tested, electrochemical impedance spectroscopy (EIS) was conducted. The EIS data fitted using an equivalent model circuit (**Figure S14a**) revealed that all the materials tested had comparable R_s values (**Table S1**). a-Si and a-Si_{0.5}Ge_{0.5} had higher R_{ct} of 2537 Ohm and 1681 Ohm after the 1st desodiation cycle as compared to the very low R_{ct} value of 49.48 ohm for a-Ge (**Figure 4f, S14b, c**). Unlike a-Si, the R_{ct} of a-Si_{0.5}Ge_{0.5} continuously decreased with increasing cycle no. to 190 ohm after 50 cycles, which signified good active material contact with the current collector and stable SEI formation during cycling (**Table S1**). In comparison, the R_{ct} of a-Ge increased considerably to 2892 Ohm after 50 cycles, consistent with significant electrode degradation during cycling, which resulted in poor electrochemical performance. EIS technique along with probing cell resistance, can further be used to calculate apparent Na-ion diffusivity coefficient

(D_{Na^+}) during various cycles.^{53–56} Therefore, determination of D_{Na^+} using **Equation S1** and **Equation S2** revealed that the Na-ion diffusivity of a-Si_{0.5}Ge_{0.5} increased with the cycle no., suggesting that incorporation of Ge in Si_{0.5}Ge_{0.5} indeed increased the diffusivity of Na-ion in the alloy structure (**Figure 4g, Table S2**). The Na-ion diffusivity increased up to $19.78 \times 10^{-18} \text{ cm}^2 \text{ s}^{-1}$ for a-Si_{0.5}Ge_{0.5}, which is 15 times higher than the Na-ion diffusivity of a-Si ($3.72 \times 10^{-18} \text{ cm}^2 \text{ s}^{-1}$) after 50 cycles (**Figure 4h**). Interestingly, the Na-ion diffusivity of a-Ge was still the highest (i.e. $28.65 \times 10^{-18} \text{ cm}^2 \text{ s}^{-1}$) after 50 cycles, however, the huge increase in the R_{ct} value explained the diminished cycle performance compared to a-Si_{0.5}Ge_{0.5} (**Figure S14d,e & Table S2**).

The SEM images of delithiated (10 cycles) and desodiated (100 cycles) a-Si_{0.5}Ge_{0.5} and a-Ge electrodes are shown in **Figure 5**. After delithiation, the cycled electrodes of a-Si_{0.5}Ge_{0.5} (**Figure 5a, e**) and a-Ge (**Figure 5c, g**) showed meshed structures with retained NW outlines as well as good adhesion with the current collector. Once cycled in a NIB for 100 cycles, the a-Si_{0.5}Ge_{0.5} (**Figure 5b, f**) and a-Ge (**Figure 5d, h**) still retained islands of cycled NWs. However, a-Ge underwent clear exfoliation from the current collector (**Figure 5d**) as compared to the well-adhered a-Si_{0.5}Ge_{0.5} NWs after 100 cycles. This was earlier reflected in EIS analysis of a-Ge (**Figure S14, Table S2**), which suggested increasing R_{ct} value with no. of cycles as compared to a-Si_{0.5}Ge_{0.5}. Here, it is possible that due to the lower degree of activation of Si in a-Si_{0.5}Ge_{0.5} alloy, the volume expansion of the NWs is reduced compared to a-Ge (volume expansion – 225 % for NaGe phase⁵⁰ as compared to 114 % for Na_{0.76}Si phase²⁷) which avoided the material pulverization during sodiation/de-sodiation. For pure a-Ge, this large volume expansion leads to poor electrode integrity and rapid capacity decay. Also in comparison to sodiated states of a-Si_{0.5}Ge_{0.5} (**Figure S15a, b**) and a-Ge (**Figure S15c, d**) post 100 cycles, the desodiated states (**Figure 5 b,f,d & h**) overall showed wider crack appearance probably due to the volume contraction after desodiation. The post-mortem TEM analysis of a-Si_{0.5}Ge_{0.5}

(**Figure 5i**) and a-Ge (**Figure 5j**) demonstrated that after 100 cycles, significant structural deformation of NWs had taken place in the latter. Also shown in inset, the diffraction pattern suggested the presence of a completely amorphous phase of both a-Si_{0.5}Ge_{0.5} alloy and pure a-Ge in the desodiated state. Further, post-mortem XRD analysis of a-Si_{0.5}Ge_{0.5} and a-Ge also confirmed that no crystalline phases were present (except SS foil substrate), post cycling (**Figure S16**). The scanning-TEM (STEM) image with corresponding mapping profile of a-Si_{0.5}Ge_{0.5} and a-Ge confirmed that Si and Ge were homogeneously distributed in the NW, post 100 cycles. The uniform Na distribution in cycled NWs is likely due to the Na based species present in the SEI layer as discussed in XPS analysis of delithiated and desodiated state of the a-Si_{0.5}Ge_{0.5} alloy (**Figure S17**).

Conclusions

In this report, we have demonstrated Na insertion in a-Si_xGe_{1-x} alloy NWs, facilitated by Li-driven amorphization of the active material. This amorphization was a crucial step in facilitating reversible Na-ion cycling, with the pristine crystalline NWs not capable of delivering appreciable capacity. We have also shown that the incorporation of Ge in Si as an alloying element is a key route for unlocking the cycling ability of pure Si NWs, which even in the a-Si state struggled to activate in a NIB. Increasing the Ge content in the alloy results in the a-Si_xGe_{1-x} NW activation, with some compositions (i.e. a-Si_{0.5}Ge_{0.5} and a-Si_{0.25}Ge_{0.75}) outperforming a-Ge cyclic performance. Among the compositions tested, the optimum Si_xGe_{1-x} alloy composition was found to be Si_{0.5}Ge_{0.5} in terms of cyclic stability in a NIB. EIS analysis suggests that enhanced Na-ion diffusivity in the amorphous state enables the Na insertion/de-insertion in the alloy NWs. The SEM and TEM analysis suggested good structural integrity of a-Si_{0.5}Ge_{0.5} electrode compared to pure a-Ge, which resulted in enhanced cycling performance for the former. This report highlights the synergistic benefits of having Si and Ge together

within an alloy, to enhance and stabilize the electrochemical performance as compared to their parent phases in a NIB.

Conflicts of interest

There are no conflicts to declare.

Acknowledgements

This project is supported by Science foundation Ireland under grant no. 18/SIRG/5484. This work was further supported by Science Foundation Ireland (SFI) under the Principal Investigator Program under contract no. 16/IA/4629. K. M. R. further acknowledges IRCLA/2017/285 and SFI Research Centres MaREI, AMBER, and CONFIRM 12/RC/2278_P2, 12/RC/2302_P2, and 16/RC/3918.

References

- (1) Chayambuka, K.; Mulder, G.; Danilov, D. L.; Notten, P. H. L. From Li-Ion Batteries toward Na-Ion Chemistries: Challenges and Opportunities. *Adv. Energy Mater.* 2020, 10, 2001310.
- (2) Vaalma, C.; Buchholz, D.; Weil, M.; Passerini, S. A Cost and Resource Analysis of Sodium-Ion Batteries. *Nat. Rev. Mater.* 2018, 3, 18013.
- (3) Nayak, P. K.; Yang, L.; Brehm, W.; Adelhelm, P. From Lithium-Ion to Sodium-Ion Batteries: Advantages, Challenges, and Surprises. *Angew. Chemie - Int. Ed.* 2018, 57, 102.
- (4) Grey, C. P.; Tarascon, J. M. Sustainability and in Situ Monitoring in Battery Development. *Nat. Mater.* 2016, 16, 45.
- (5) Hwang, J. Y.; Myung, S. T.; Sun, Y. K. Sodium-Ion Batteries: Present and Future. *Chem. Soc. Rev.* 2017, 46, 3529.
- (6) Lee, B.; Paek, E.; Mitlin, D.; Lee, S. W. Sodium Metal Anodes: Emerging Solutions to Dendrite Growth. *Chem. Rev.* 2019, 119, 5416.
- (7) Zhang, J. G.; Xu, W.; Xiao, J.; Cao, X.; Liu, J. Lithium Metal Anodes with Nonaqueous Electrolytes. *Chem. Rev.* 2020, 120, 13312.
- (8) Jache, B.; Adelhelm, P. Use of Graphite as a Highly Reversible Electrode with Superior Cycle Life for Sodium-Ion Batteries by Making Use of Co-Intercalation Phenomena. *Angew. Chemie - Int. Ed.* 2014, 53, 10169.
- (9) Zhao, L. F.; Hu, Z.; Lai, W. H.; Tao, Y.; Peng, J.; Miao, Z. C.; Wang, Y. X.; Chou, S. L.; Liu, H. K.; Dou, S. X. Hard Carbon Anodes: Fundamental Understanding and Commercial

Perspectives for Na-Ion Batteries beyond Li-Ion and K-Ion Counterparts. *Adv. Energy Mater.* 2021, 11, 2002704.

(10) Dou, X.; Hasa, I.; Saurel, D.; Vaalma, C.; Wu, L.; Buchholz, D.; Bresser, D.; Komaba, S.; Passerini, S. Hard Carbons for Sodium-Ion Batteries: Structure, Analysis, Sustainability, and Electrochemistry. *Mater. Today* 2019, 23, 87.

(11) Yang, X.; Rogach, A. L. Anodes and Sodium-Free Cathodes in Sodium Ion Batteries. *Adv. Energy Mater.* 2020, 10 (22), 2000288.

(12) McSweeney, W.; Geaney, H.; O'Dwyer, C. Metal-Assisted Chemical Etching of Silicon and the Behavior of Nanoscale Silicon Materials as Li-Ion Battery Anodes. *Nano Res.* 2015, 8, 1395–1442.

(13) Kennedy, T.; Brandon, M.; Ryan, K. M. Advances in the Application of Silicon and Germanium Nanowires for High-Performance Lithium-Ion Batteries. *Adv. Mater.* 2016, 28, 5696–5704.

(14) Wang, W.; Li, W.; Wang, S.; Miao, Z.; Liu, H. K.; Chou, S. Structural Design of Anode Materials for Sodium-Ion Batteries. *J. Mater. Chem. A* 2018, 6, 6183.

(15) Loaiza, L. C.; Monconduit, L.; Seznec, V. Si and Ge-Based Anode Materials for Li-, Na-, and K-Ion Batteries: A Perspective from Structure to Electrochemical Mechanism. *Small* 2020, 16, 1905260.

(16) Aminu, I. S.; Geaney, H.; Imtiaz, S.; Adegoke, T. E.; Kapuria, N.; Collins, G. A.; Ryan, K. M. A Copper Silicide Nanofoam Current Collector for Directly Grown Si Nanowire Networks and Their Application as Lithium-Ion Anodes. *Adv. Funct. Mater.* 2020, 30, 2003278.

- (17) Geaney, H.; Bree, G.; Stokes, K.; McCarthy, K.; Kennedy, T.; Ryan, K. M. Highlighting the Importance of Full-Cell Testing for High Performance Anode Materials Comprising Li Alloying Nanowires. *J. Electrochem. Soc.* 2019, 166, A2784.
- (18) Collins, G. A.; McNamara, K.; Kilian, S.; Geaney, H.; Ryan, K. M. Alloying Germanium Nanowire Anodes Dramatically Outperform Graphite Anodes in Full-Cell Chemistries over a Wide Temperature Range. *ACS Appl. Energy Mater.* 2021, 4, 1793.
- (19) Yang, Y.; Yuan, W.; Kang, W.; Ye, Y.; Pan, Q.; Zhang, X.; Ke, Y.; Wang, C.; Qiu, Z.; Tang, Y. A Review on Silicon Nanowire-Based Anodes for next-Generation High-Performance Lithium-Ion Batteries from a Material-Based Perspective. *Sustain. Energy Fuels* 2020, 4, 1577.
- (20) Cui, L. F.; Yang, Y.; Hsu, C. M.; Yi, C. Carbon-Silicon Core-Shell Nanowires as High Capacity Electrode for Lithium Ion Batteries. *Nano Lett.* 2009, 9, 3370.
- (21) Mullane, E.; Kennedy, T.; Geaney, H.; Ryan, K. M. A Rapid, Solvent-Free Protocol for the Synthesis of Germanium Nanowire Lithium-Ion Anodes with a Long Cycle Life and High Rate Capability. *ACS Appl. Mater. Interfaces* 2014, 6, 18800.
- (22) Stojić, M.; Kostić, D.; Stošić, B. The Behaviour of Sodium in Ge, Si and GaAs. *Phys. B+C* 1986, 138, 125.
- (23) Kulish, V. V.; Malyi, O. I.; Ng, M. F.; Chen, Z.; Manzhos, S.; Wu, P. Controlling Na Diffusion by Rational Design of Si-Based Layered Architectures. *Phys. Chem. Chem. Phys.* 2014, 16, 4260.

- (24) Legrain, F.; Malyi, O. I.; Manzhos, S. Comparative Computational Study of the Energetics of Li, Na, and Mg Storage in Amorphous and Crystalline Silicon. *Comput. Mater. Sci.* 2014, 94, 214.
- (25) Kohandehghan, A.; Cui, K.; Kupsta, M.; Ding, J.; Memarzadeh Lotfabad, E.; Kalisvaart, W. P.; Mitlin, D. Activation with Li Enables Facile Sodium Storage in Germanium. *Nano Lett.* 2014, 14, 5873.
- (26) Jangid, M. K.; Lakhnot, A. S.; Vemulapally, A.; Sonia, F. J.; Sinha, S.; Dusane, R. O.; Mukhopadhyay, A. Crystalline Core/Amorphous Shell Structured Silicon Nanowires Offer Size and Structure Dependent Reversible Na-Storage. *J. Mater. Chem. A* 2018, 6, 3422.
- (27) Jung, S. C.; Jung, D. S.; Choi, J. W.; Han, Y. K. Atom-Level Understanding of the Sodiation Process in Silicon Anode Material. *J. Phys. Chem. Lett.* 2014, 5, 1283.
- (28) Xu, Y.; Swaans, E.; Basak, S.; Zandbergen, H. W.; Borsa, D. M.; Mulder, F. M. Reversible Na-Ion Uptake in Si Nanoparticles. *Adv. Energy Mater.* 2016, 6, 1501436.
- (29) Huang, S.; Liu, L.; Zheng, Y.; Wang, Y.; Kong, D.; Zhang, Y.; Shi, Y.; Zhang, L.; Schmidt, O. G.; Yang, H. Y. Efficient Sodium Storage in Rolled-Up Amorphous Si Nanomembranes. *Adv. Mater.* 2018, 30, 1706637.
- (30) Lim, C. H.; Huang, T. Y.; Shao, P. S.; Chien, J. H.; Weng, Y. T.; Huang, H. F.; Hwang, B. J.; Wu, N. L. Experimental Study on Sodiation of Amorphous Silicon for Use as Sodium-Ion Battery Anode. *Electrochim. Acta* 2016, 211, 265.
- (31) Abel, P. R.; Lin, Y. M.; De Souza, T.; Chou, C. Y.; Gupta, A.; Goodenough, J. B.; Hwang, G. S.; Heller, A.; Mullins, C. B. Nanocolumnar Germanium Thin Films as a High-Rate Sodium-Ion Battery Anode Material. *J. Phys. Chem. C* 2013, 117, 18885.

- (32) Wu, H.; Liu, W.; Zheng, L.; Zhu, D.; Du, N.; Xiao, C.; Su, L.; Wang, L. Facile Synthesis of Amorphous Ge Supported by Ni Nanopyramid Arrays as an Anode Material for Sodium-Ion Batteries. *ChemistryOpen* 2019, 8, 298.
- (33) Kalisvaart, W. P.; Olsen, B. C.; Luber, E. J.; Buriak, J. M. Sb-Si Alloys and Multilayers for Sodium-Ion Battery Anodes. *ACS Appl. Energy Mater.* 2019, 2, 2205.
- (34) Sayed, S. Y.; Kalisvaart, W. P.; Luber, E. J.; Olsen, B. C.; Buriak, J. M. Stabilizing Tin Anodes in Sodium-Ion Batteries by Alloying with Silicon. *ACS Appl. Energy Mater.* 2020, 3, 9950.
- (35) Abel, P. R.; Fields, M. G.; Heller, A.; Mullins, C. B. Tin-Germanium Alloys as Anode Materials for Sodium-Ion Batteries. *ACS Appl. Mater. Interfaces* 2014, 6, 15860.
- (36) Farbod, B.; Cui, K.; Kalisvaart, W. P.; Kupsta, M.; Zehri, B.; Kohandehghan, A.; Lotfabad, E. M.; Li, Z.; Luber, E. J.; Mitlin, D. Anodes for Sodium Ion Batteries Based on Tin-Germanium-Antimony Alloys. *ACS Nano* 2014, 8, 4415.
- (37) Loaiza, L. C.; Salager, E.; Louvain, N.; Boulaoued, A.; Iadecola, A.; Johansson, P.; Stievano, L.; Seznec, V.; Monconduit, L. Understanding the Lithiation/Delithiation Mechanism of Si_{1-x}Gex Alloys. *J. Mater. Chem. A* 2017, 5, 12462.
- (38) Abel, P. R.; Chockla, A. M.; Lin, Y. M.; Holmberg, V. C.; Harris, J. T.; Korgel, B. A.; Heller, A.; Mullins, C. B. Nanostructured Si(1- x)Gex for Tunable Thin Film Lithium-Ion Battery Anodes. *ACS Nano* 2013, 3, 2249.
- (39) Stokes, K.; Geaney, H.; Flynn, G.; Sheehan, M.; Kennedy, T.; Ryan, K. M. Direct Synthesis of Alloyed Si_{1-x}Gex Nanowires for Performance-Tunable Lithium Ion Battery Anodes. *ACS Nano* 2017, 11, 10088.

- (40) Geaney, H.; Mullane, E.; Ramasse, Q. M.; Ryan, K. M. Atomically Abrupt Silicon-Germanium Axial Heterostructure Nanowires Synthesized in a Solvent Vapor Growth System. *Nano Lett.* 2013, 13, 1675.
- (41) Lee, W. J.; Ma, J. W.; Bae, J. M.; Park, S. H.; Cho, M. H.; Ahn, J. P. The Modulation of Si₁-XGe_x Nanowires by Correlation of Inlet Gas Ratio with H₂ Gas Content. *CrystEngComm* 2011, 13, 5204.
- (42) Geaney, H.; Kennedy, T.; Dickinson, C.; Mullane, E.; Singh, A.; Laffir, F.; Ryan, K. M. High Density Growth of Indium Seeded Silicon Nanowires in the Vapor Phase of a High Boiling Point Solvent. *Chem. Mater.* 2012, 22, 2204.
- (43) Mullane, E.; Kennedy, T.; Geaney, H.; Dickinson, C.; Ryan, K. M. Synthesis of Tin Catalyzed Silicon and Germanium Nanowires in a Solvent-Vapor System and Optimization of the Seed/Nanowire Interface for Dual Lithium Cycling. *Chem. Mater.* 2013, 25, 1816.
- (44) McDowell, M. T.; Lee, S. W.; Ryu, I.; Wu, H.; Nix, W. D.; Choi, J. W.; Cui, Y. Novel Size and Surface Oxide Effects in Silicon Nanowires as Lithium Battery Anodes. *Nano Lett.* 2011, 11, 4018.
- (45) Bogart, T. D.; Oka, D.; Lu, X.; Gu, M.; Wang, C.; Korgel, B. A. Lithium Ion Battery Performance of Silicon Nanowires with Carbon Skin. *ACS Nano* 2014, 8 (1), 915–922.
- (46) Stokes, K.; Flynn, G.; Geaney, H.; Bree, G.; Ryan, K. M. Axial Si-Ge Heterostructure Nanowires as Lithium-Ion Battery Anodes. *Nano Lett.* 2018, 18, 5569.
- (47) Kennedy, T.; Mullane, E.; Geaney, H.; Osiak, M.; O'Dwyer, C.; Ryan, K. M. High-Performance Germanium Nanowire-Based Lithium-Ion Battery Anodes Extending over 1000 Cycles through in Situ Formation of a Continuous Porous Network. *Nano Lett.* 2014, 14, 716.

- (48) Liu, X. H.; Huang, S.; Picraux, S. T.; Li, J.; Zhu, T.; Huang, J. Y. Reversible Nanopore Formation in Ge Nanowires during Lithiation- Delithiation Cycling: An in Situ Transmission Electron Microscopy Study. *Nano Lett.* 2011, 11, 3991.
- (49) Lu, X.; Bogart, T. D.; Gu, M.; Wang, C.; Korgel, B. A. In Situ TEM Observations of Sn-Containing Silicon Nanowires Undergoing Reversible Pore Formation Due to Fast Lithiation/Delithiation Kinetics. *J. Phys. Chem. C* 2015, 119, 21889.
- (50) Lu, X.; Adkins, E. R.; He, Y.; Zhong, L.; Luo, L.; Mao, S. X.; Wang, C. M.; Korgel, B. A. Germanium as a Sodium Ion Battery Material: In Situ TEM Reveals Fast Sodiation Kinetics with High Capacity. *Chem. Mater.* 2016, 28, 1236.
- (51) Qin, B.; Schiele, A.; Jusys, Z.; Mariani, A.; Diemant, T.; Liu, X.; Brezesinski, T.; Behm, R. J.; Varzi, A.; Passerini, S. Highly Reversible Sodiation of Tin in Glyme Electrolytes: The Critical Role of the Solid Electrolyte Interphase and Its Formation Mechanism. *ACS Appl. Mater. Interfaces* 2020, 12, 3697.
- (52) Sharma, V.; Ghatak, K.; Datta, D. Amorphous Germanium as a Promising Anode Material for Sodium Ion Batteries: A First Principle Study. *J. Mater. Sci.* 2018, 53, 14423.
- (53) Cao, L.; Gao, X.; Zhang, B.; Ou, X.; Zhang, J.; Luo, W. Bin. Bimetallic Sulfide Sb₂S₃@FeS₂ Hollow Nanorods as High-Performance Anode Materials for Sodium-Ion Batteries. *ACS Appl. Mater. Interfaces* 2020, 14, 3610–3620.
- (54) Ran, L.; Luo, B.; Gentle, I. R.; Lin, T.; Sun, Q.; Li, M.; Rana, M. M.; Wang, L.; Knibbe, R. Biomimetic Sn₄P₃ Anchored on Carbon Nanotubes as an Anode for High-Performance Sodium-Ion Batteries. *ACS Nano* 2020, 14 (7), 8826–8837.

- (55) Li, Y.; Qian, J.; Zhang, M.; Wang, S.; Wang, Z.; Li, M.; Bai, Y.; An, Q.; Xu, H.; Wu, F.; Mai, L.; Wu, C. Co-Construction of Sulfur Vacancies and Heterojunctions in Tungsten Disulfide to Induce Fast Electronic/Ionic Diffusion Kinetics for Sodium-Ion Batteries. *Adv. Mater.* 2020, 32 (47), 1–9.
- (56) Zhao, W.; Gao, L.; Yue, L.; Wang, X.; Liu, Q.; Luo, Y.; Li, T.; Shi, X.; Asiri, A. M.; Sun, X. Constructing a Hollow Microflower-like ZnS/CuS@C Heterojunction as an Effective Ion-Transport Booster for an Ultrastable and High-Rate Sodium Storage Anode. *J. Mater. Chem. A* 2021, 9 (10), 6402–6412.

Supporting information

Syed Abdul Ahad , Seamus Kilian , Maria Zubair , Vasily A. Lebedev , Karrina McNamara , Kevin M. Ryan , Tadhg Kennedy and Hugh Geaney*

*Department of Chemical Sciences and Bernal Institute, University of Limerick, Limerick V94 T9PX, Ireland. E-mail: Hugh.Geaney@ul.ie

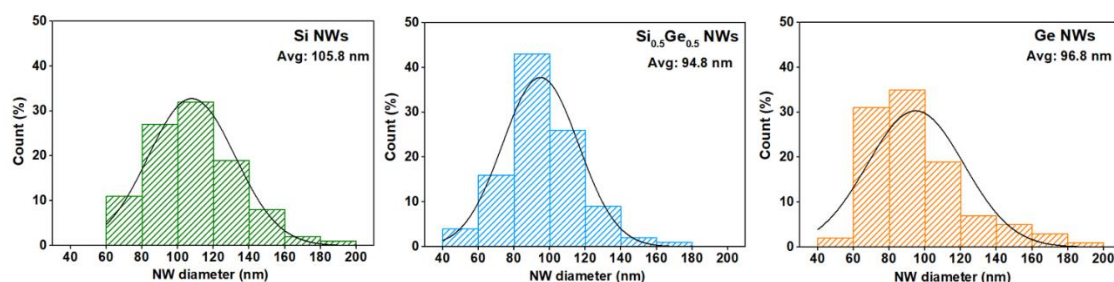


Figure S1 Histogram of diameter distribution of Si, Si_{0.5}Ge_{0.5} and Ge NWs respectively

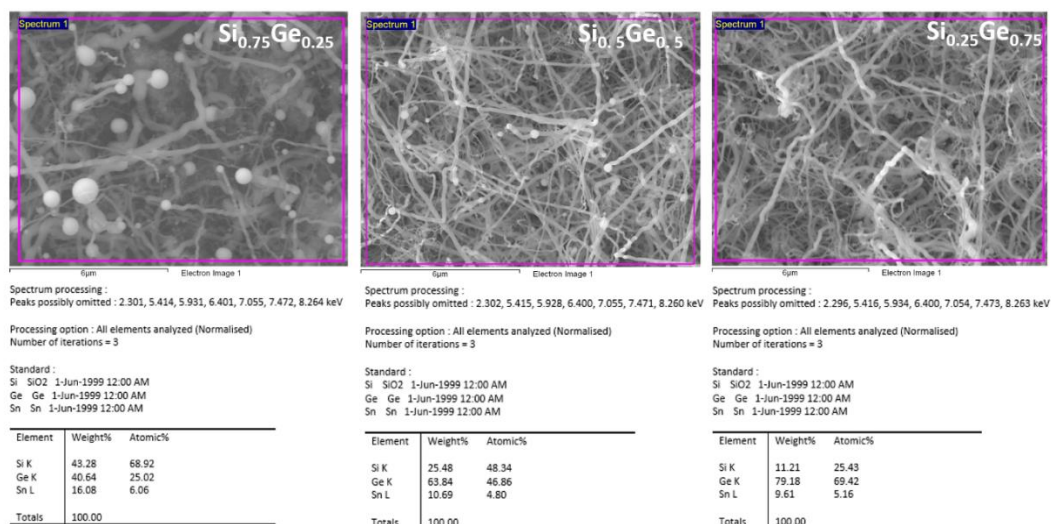


Figure S2 EDS data of Si_{0.75}Ge_{0.25}, Si_{0.5}Ge_{0.5} and Si_{0.25}Ge_{0.75} NWs with corresponding atomic and weight ratios of Si, Ge and Sn.

Please note that the above listed compositions contain 4-6 at. % Sn as well which is coming from 20 nm Sn seed catalyst used to grow Si_xGe_{1-x} NWs using SLS method. Therefore, the complete nomenclature of these compositions can be written as Si_{0.6892}Ge_{0.2502}Sn_{0.0606}, Si_{0.4834}Ge_{0.4686}Sn_{0.0480} and Si_{0.2545}Ge_{0.6942}Sn_{0.0516}. However, for simplicity, the compositions are listed based on the nearest Si and Ge composition such as Si_{0.75}Ge_{0.25}, Si_{0.5}Ge_{0.5} and Si_{0.25}Ge_{0.75} respectively.

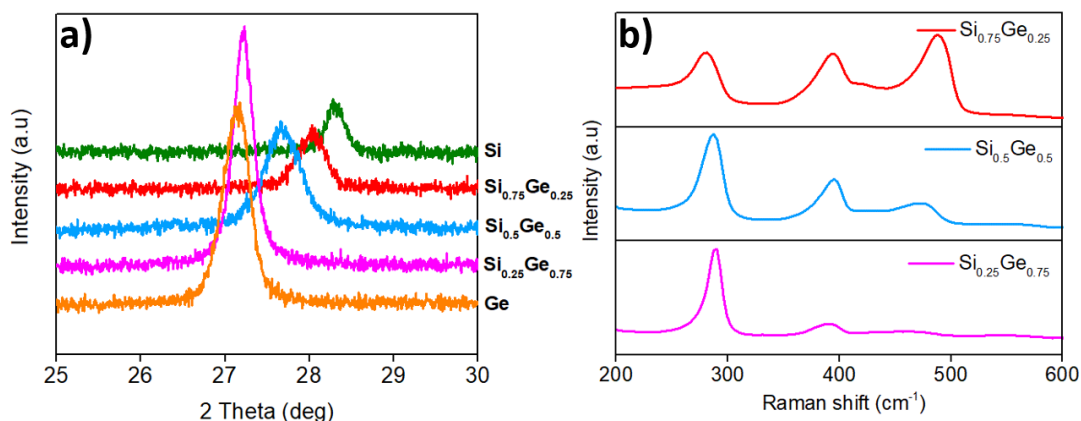


Figure S3 (a) XRD analysis of different alloy compositions, pure Si and pure Ge phases between $25^\circ - 30^\circ$ to show clear shift in (111) peak shift. (b) Raman spectra of different alloy compositions and the corresponding shift in Si-Si, Si-Ge and Ge-Ge active modes.

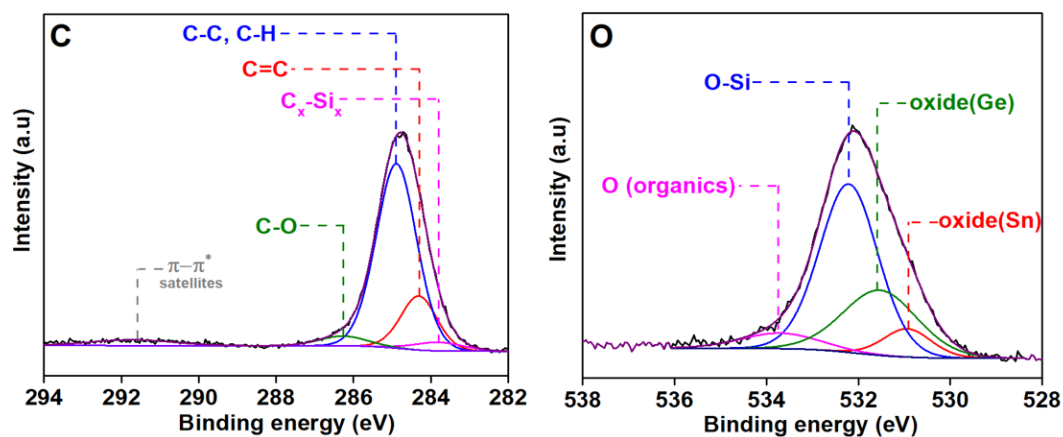


Fig S4 XPS core-level spectra of C and O of $\text{Si}_{0.5}\text{Ge}_{0.5}$ NW.

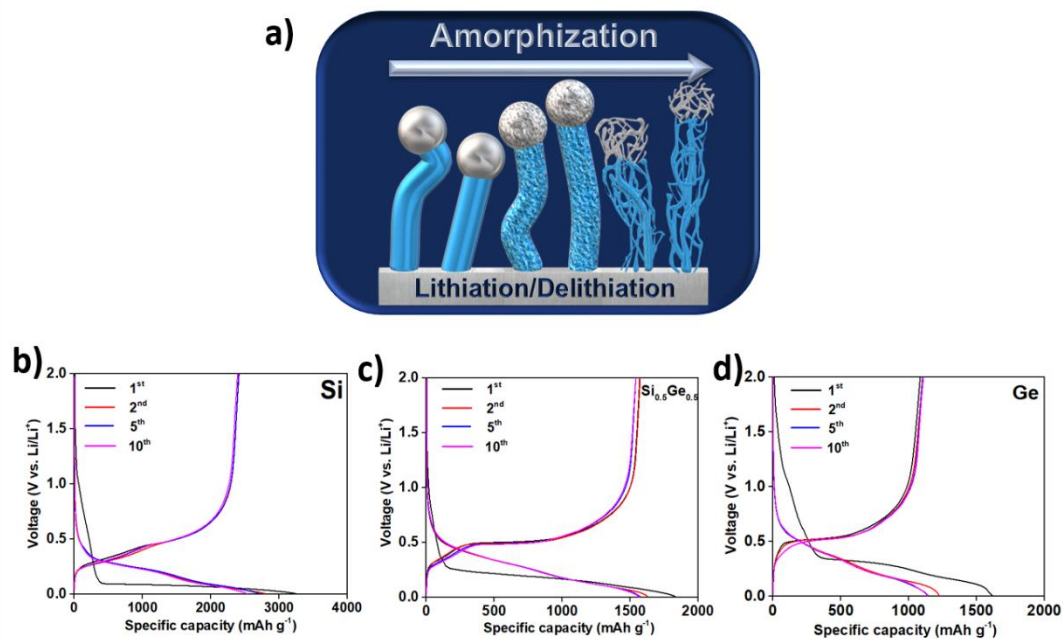


Fig S5 (a) Schematic illustration of amorphization step of crystalline NW in a LIB. Voltage-capacity profile of (a) Si, (b) Si_{0.5}Ge_{0.5} and (c) Ge NWs cycled in a LIB between 0.005-2.0 V at C/5 rate.

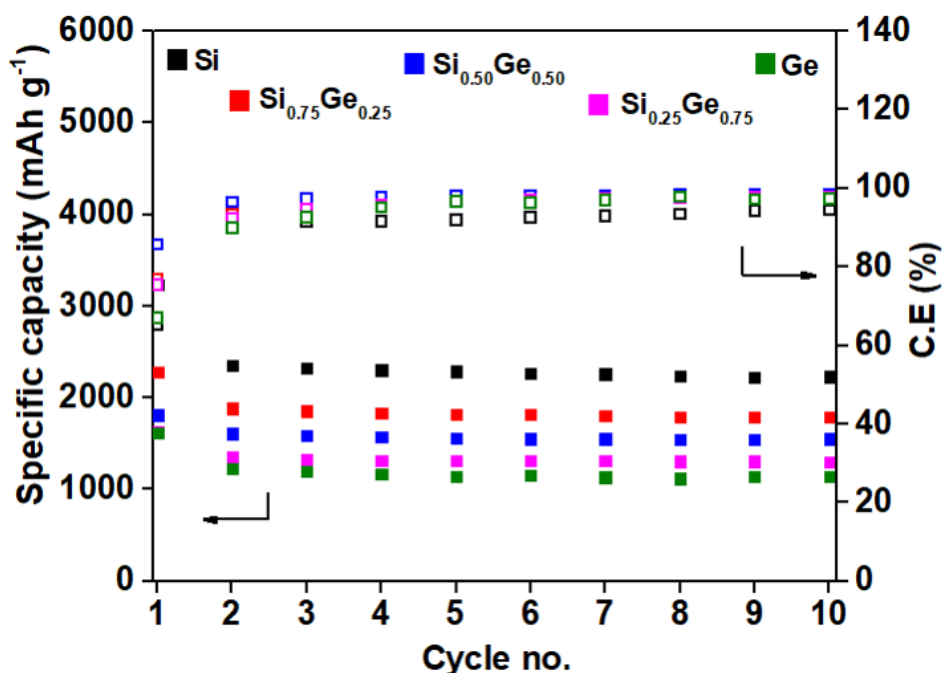


Figure S6 Cyclic performance of pure Si, pure Ge and different Si_xGe_{1-x} alloy NW compositions cycled in a LIB between 0.005 – 2.0 V at C/5 rate.

The first cycle lithiation capacity obtained was 3231.1 mAh g⁻¹, 2282 mAh g⁻¹, 1811.8 mAh g⁻¹, 1630.95 mAh g⁻¹ and 1615.3 mAh g⁻¹ for Si, Si_{0.75}Ge_{0.25}, Si_{0.50}Ge_{0.50}, Si_{0.25}Ge_{0.75} and Ge respectively which included 1st cycle lithiation as well as capacity derived from the formation of solid-electrolyte interface (SEI) layer. Subsequently after 10 cycles, lithiation capacity was 2228.85 mAh g⁻¹, 1788.64 mAh g⁻¹, 1550.25 mAh g⁻¹, 1301.96 mAh g⁻¹ and 1137.77 mAh g⁻¹ for Si, Si_{0.75}Ge_{0.25}, Si_{0.50}Ge_{0.50}, Si_{0.25}Ge_{0.75} and Ge respectively, with coulombic efficiency ranging from 94 % – 97 % for all the alloys and parent phases. The slightly lower specific capacity obtained in the subsequent cycles might be due to the irreversible alloying with the oxide species, also highlighted in XPS analysis (**Figure 2f-h**).¹

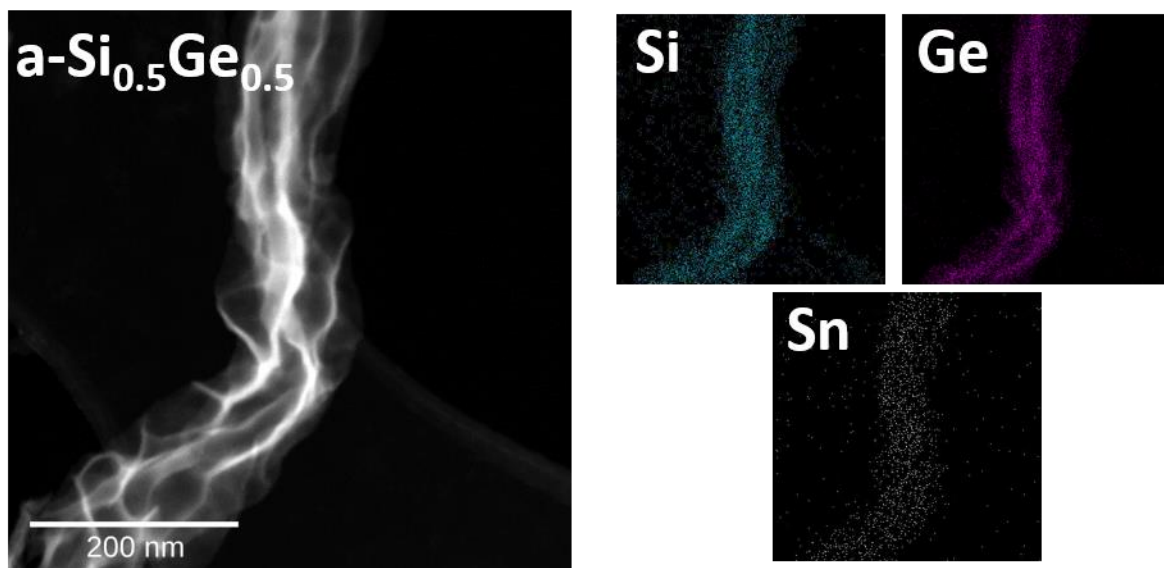


Figure S7 STEM image and corresponding EDX mapping of Si, Ge and Sn elemental distribution in de-lithiated $\text{Si}_{0.5}\text{Ge}_{0.5}$ NW.

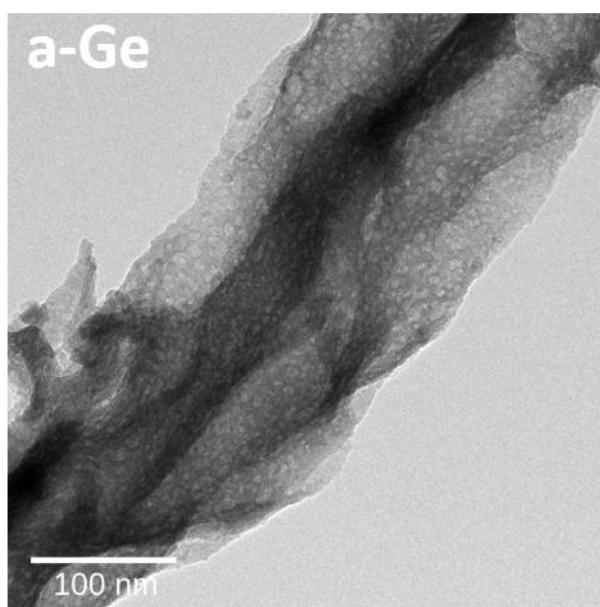


Figure S8 High magnification TEM image showing nanopores in de-lithiated a-Ge NW.

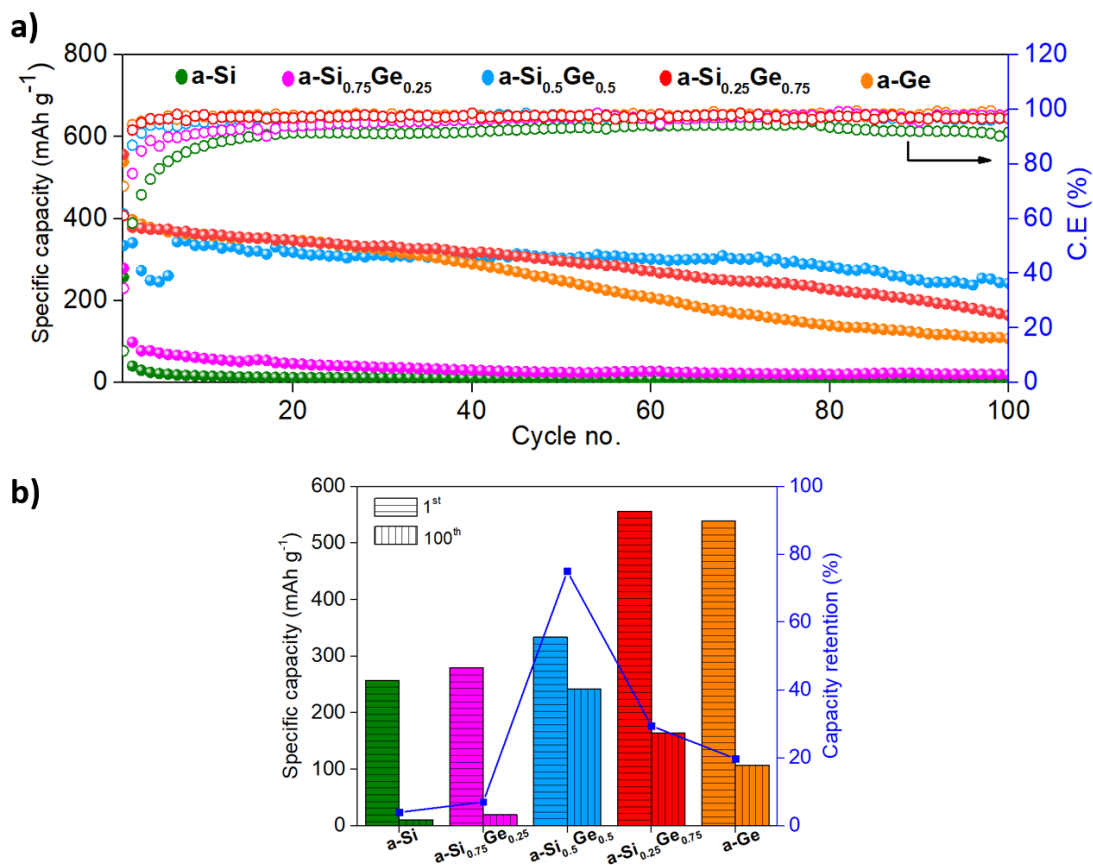


Figure S9 (a) Specific capacity vs. cycle no. and (b) Comparison of specific capacity retention between 1st and 100th cycle of a-Si, a-Ge and various a-Si_xGe_{1-x} alloy compositions cycled between 0.005-2.0 V at 50 mA g⁻¹. The capacity retention after 100 cycles for a-Si, a-Si_{0.75}Ge_{0.25}, a-Si_{0.5}Ge_{0.5}, a-Si_{0.25}Ge_{0.75} and a-Ge was 3.93%, 7.0%, 75%, 29.4% and 19.8% respectively.

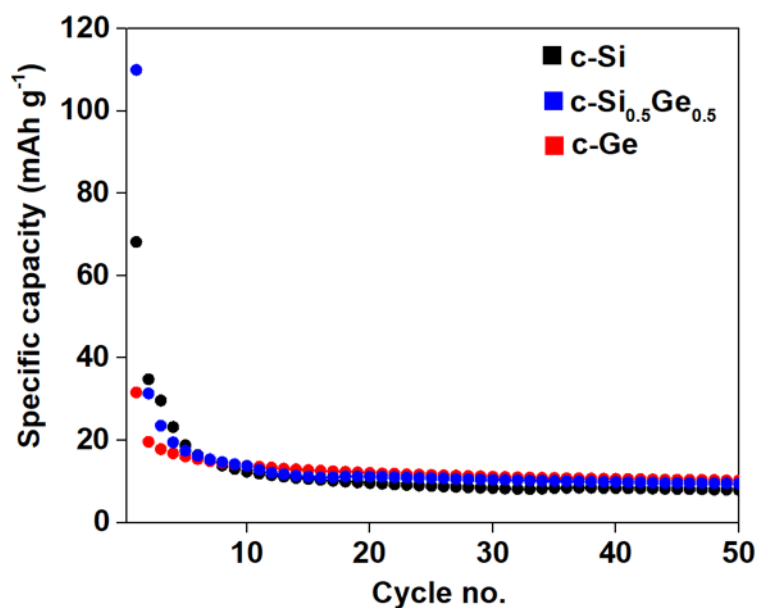


Figure S10 Specific capacity vs. cycle no. of c-Si, c-Si_{0.5}Ge_{0.5} and c-Ge cycled between 0.005-2.0 V at 50 mA g⁻¹ in a NIB.

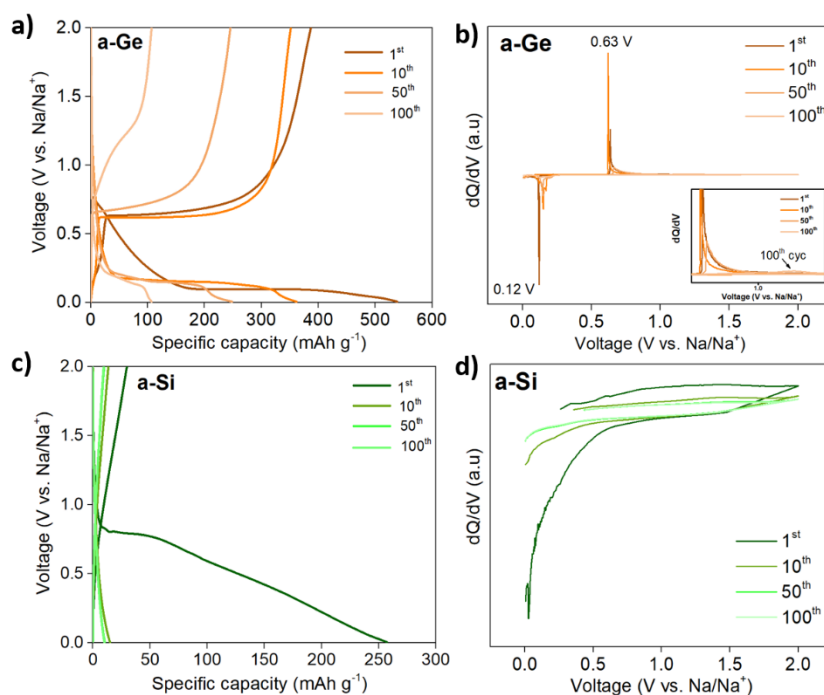


Figure S11 Voltage - capacity profile (a,c) and corresponding differential-capacity plot (b,d) of a-Ge and a-Si cycled between 0.005 – 2.0 V.

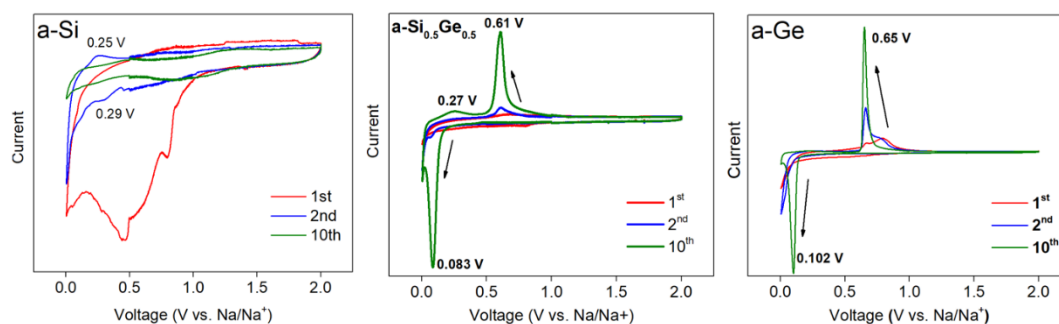


Figure S12 Cyclic voltammetry graphs of a-Si, a-Si_{0.5}Ge_{0.5} and a-Ge at a scan rate of 0.02 mV s⁻¹.

The CV plots showed that after the 1st cycle, there is a broad peak around 0.29 V, consistent with Na intercalation in a-Si while the broad peak around 0.25 V can be attributed to the desodiation of Na ion from a-Si.² However, in the subsequent cycles, these peaks completely disappear, suggesting irreversible sodium insertion in the a-Si structure. The sodiation peaks appear at 0.083 and 0.102 V while the desodiation peaks appear at 0.61 V and 0.65 V for a-Si_{0.5}Ge_{0.5} and a-Ge respectively after 10 cycles. These results agree with the differential capacity plots presented in Fig 4d and Fig S11b. A broad peak appearing at 0.27 V for a-Si_{0.5}Ge_{0.5} might be due to the desodiation of Na_xSn or Na_xSi phase. However, no sodiation peaks were found which could be attributed to the formation of Na_ySn phase.

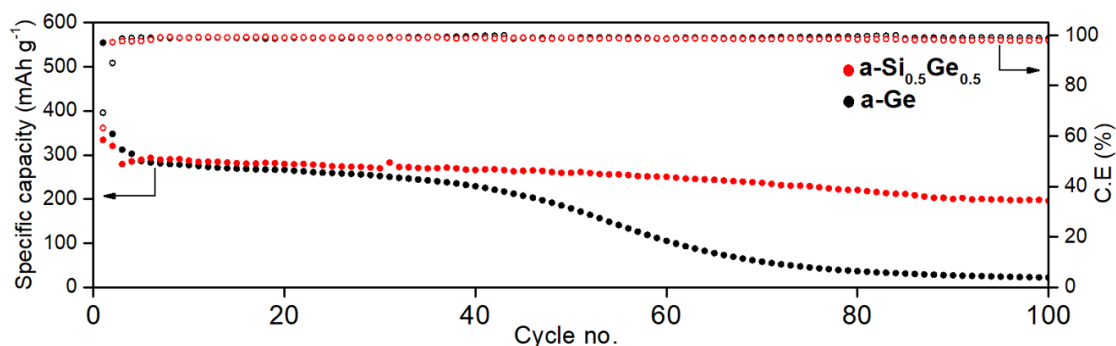


Figure S13 (a) Specific capacity vs. cycle no. of a-Si_{0.5}Ge_{0.5} and a-Ge NWs cycled between 0.005-2.0 V at 200 mA g⁻¹.

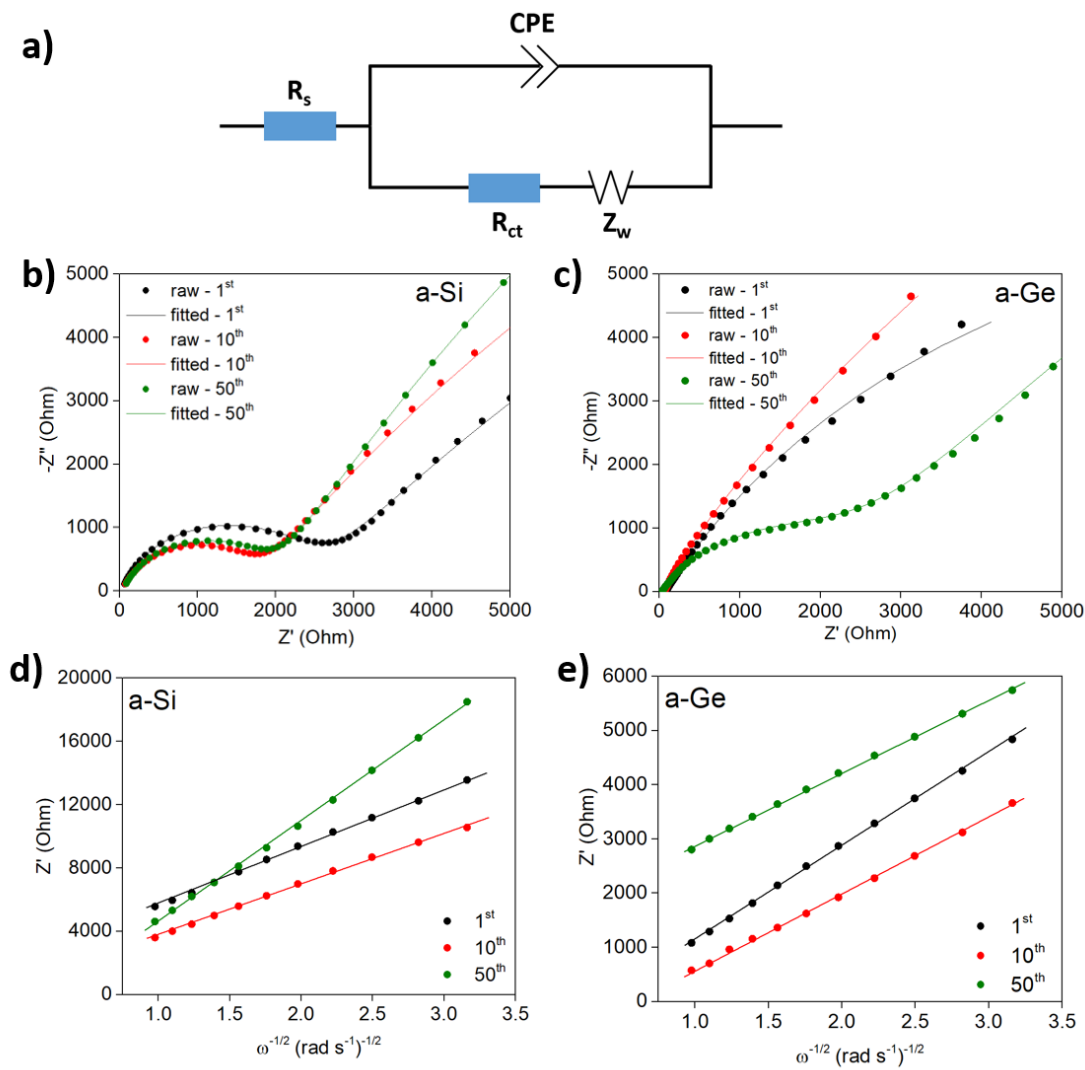


Figure S14 (a) Equivalent circuit used for fitting of EIS data. The Nyquist plots of a-Si (b) and a-Ge (c) after 1st, 10th and 50th cycle. The Z vs. $\omega^{-1/2}$ plots of a-Si (d) and a-Ge (e) derived from their corresponding Nyquist plots.

The equivalent circuit contains R_s which is the solution resistance of the cell, R_{ct} is the charge transfer resistance, CPE is the capacitance while Z_w is the Warburg factor.

	a-Si		a-Si _{0.5} Ge _{0.5}		a-Ge	
	R _s (Ohm)	R _{ct} (Ohm)	R _s (Ohm)	R _{ct} (Ohm)	R _s (Ohm)	R _{ct} (Ohm)
1 st	33.03	2537	26.25	1681	33	49.48
10 th	39.71	1813	26.33	909.5	33.5	44.65
50 th	40.48	2014	29.33	235.6	39.7	2892

Table S1 Tabulation of R_s and R_{ct} value of a-Si, a-Si_{0.5}Ge_{0.5} and a-Ge at different cycle no. cycled in a NIB.

	a-Si		a-Si _{0.5} Ge _{0.5}		a-Ge	
	D _{Na} (cm ² s ⁻¹)	σ	D _{Na} (cm ² s ⁻¹)	σ	D _{Na} (cm ² s ⁻¹)	σ
1 st	3.72 × 10 ⁻¹⁸	3764.2	7.65 × 10 ⁻¹⁸	2623.3	17.70 × 10 ⁻¹⁸	1722.9
10 th	4.37 × 10 ⁻¹⁸	3473.6	19.19 × 10 ⁻¹⁸	1657.1	26.71 × 10 ⁻¹⁸	1404.7
50 th	1.29 × 10 ⁻¹⁸	6382.7	19.78 × 10 ⁻¹⁸	1632.2	28.65 × 10 ⁻¹⁸	1356.31

Table S2 Tabulation of corresponding σ and D_{Na} values of a-Si, a-Si_{0.5}Ge_{0.5} and a-Ge at different cycle no. cycled in a NIB.

The values of σ and D_{Na} were calculated from the following equation:

Equation S1 $\rightarrow D_{Na^+} = R^2 T^2 / 2n^4 F^4 A^2 C^2 \sigma^2$

Equation S2 $\rightarrow Z' = R_s + R_{ct} + \sigma \omega^{-1/2}$

Where D_{Na}⁺, R, T, n, A, F, C and σ are Na ion Diffusion coefficient, gas constant, temperature, no. of electrons per molecule during oxidation, surface area of electrode, Faraday constant, Na ion concentration and Warburg factor (calculated using Eq. 1) respectively.

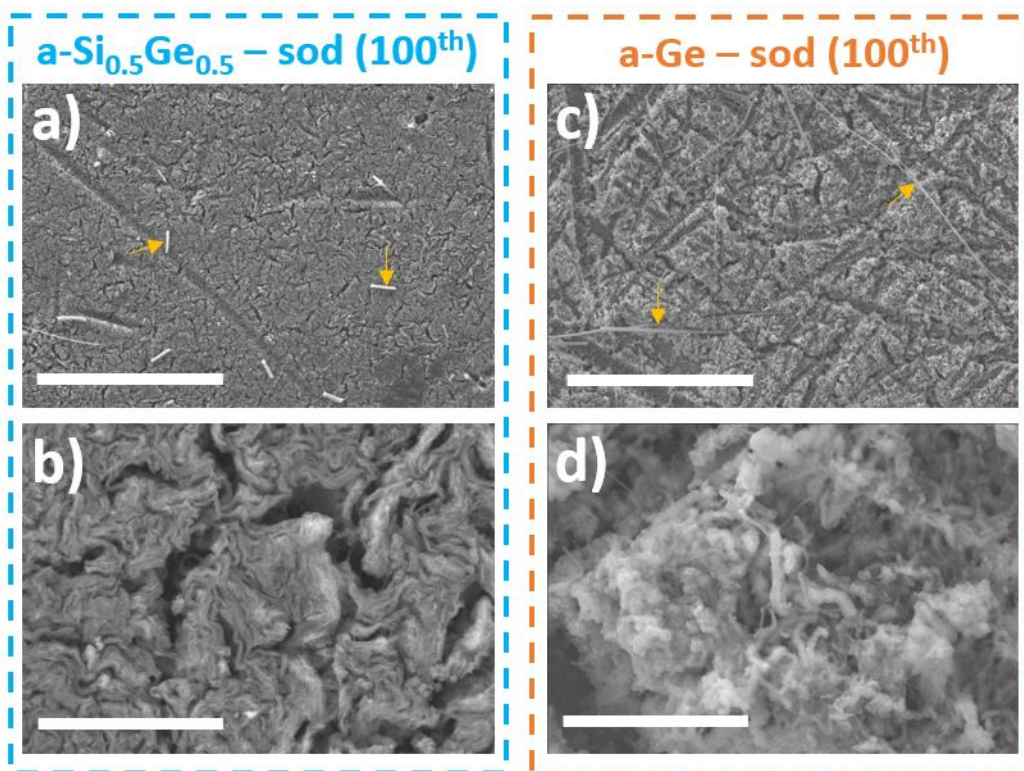


Figure S15 SEM image of (a, b) a-Si_{0.5}Ge_{0.5} -sodiated and (c, d) a-Ge – sodiated state after 100th cycle. The scale bares in a, & c represents 50 μm while scale bar in b & d represents 5 μm. The orange arrows indicate glass fibers remains from the GF/D current collector after cell disassembly.

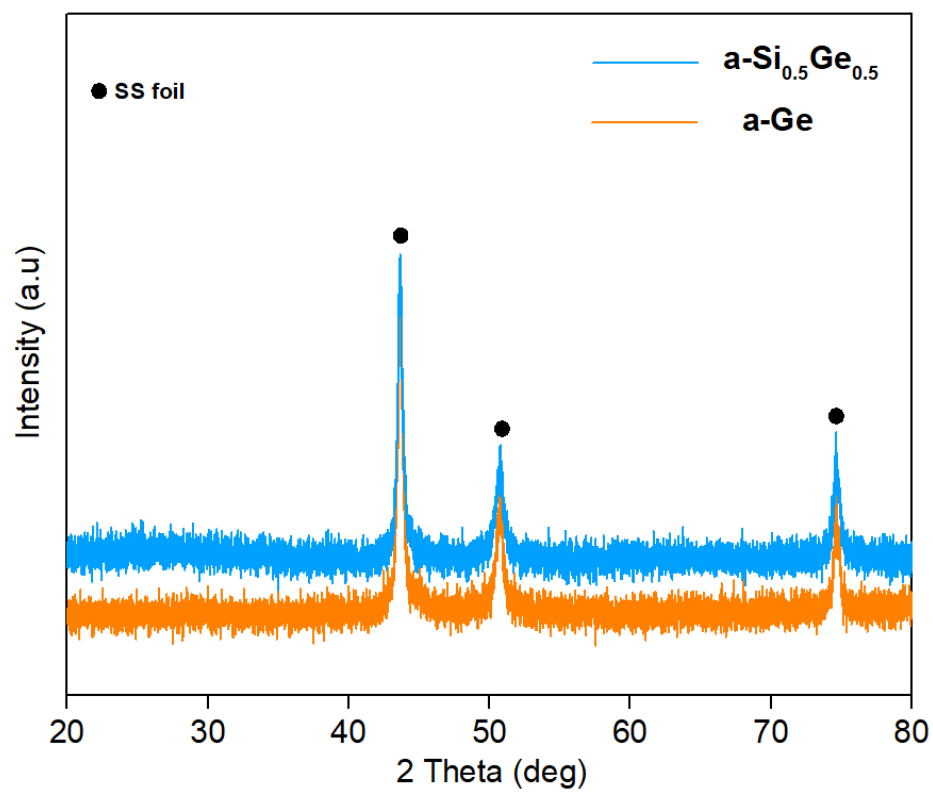


Figure S16 Post-mortem XRD analysis of $a\text{-Si}_{0.5}\text{Ge}_{0.5}$ and $a\text{-Ge}$ NW post Na-ion cycling.

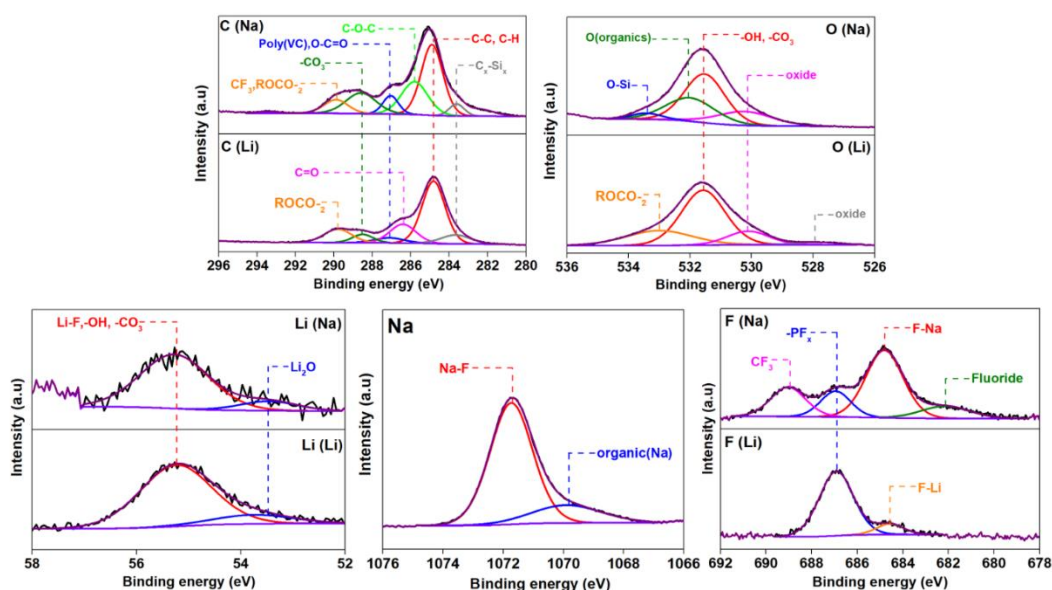


Figure S17 XPS core-level spectra of C, O, Li, Na and F in delithiated (represented by (Li)) and desodiated (represented by (Na)) state of $\text{a-Si}_{0.5}\text{Ge}_{0.5}$ NW.

A comparison of the C 1s spectra shows the typical presence of organic/inorganic species like C-C, -O-C=O (ester), C=O, C-O-C (ether), ROCO_2^- , CO_3^- (Li, Na) and CF_3 from decomposition of LiPF_6 and NaOTf salt. The O 1s spectra also shows the presence of mostly organic oxide species, corresponding to the species shown in C 1s spectra. The Li (Li) spectra reveals the presence of LiF , LiCO_3 and oxide species due to the decomposition of LiPF_6 salt and additives involved in the electrolyte. Finally apart from Na-organics presence, the Na spectra reveals the additional formation of NaF and CF_3 species from the decomposition of NaOTf salt while still showing the LiF and other Li-based inorganic species suggesting that SEI formed due to earlier lithiation/delithiation co-exists with SEI formed due to sodiation/desodiation process. Lastly, F 1s spectra confirms the presence of organic/inorganic based -F species (i.e. LiF , NaF , $-\text{CF}_3$, PF_x and fluorides from decomposed electrolyte salt) from both the delithiated and desodiated state of $\text{a-Si}_{0.5}\text{Ge}_{0.5}$ NW.^{3,4,5}

Supporting references

- (1) McDowell, M. T.; Lee, S. W.; Ryu, I.; Wu, H.; Nix, W. D.; Choi, J. W.; Cui, Y. Novel Size and Surface Oxide Effects in Silicon Nanowires as Lithium Battery Anodes. *Nano Lett.* 2011, 11, 4018.
- (2) Huang, S.; Liu, L.; Zheng, Y.; Wang, Y.; Kong, D.; Zhang, Y.; Shi, Y.; Zhang, L.; Schmidt, O. G.; Yang, H. Y. Efficient Sodium Storage in Rolled-Up Amorphous Si Nanomembranes. *Adv. Mater.* 2018, 30, 1706637.
- (3) Kennedy, T.; Brandon, M.; Laffir, F.; Ryan, K. M. Understanding the Influence of Electrolyte Additives on the Electrochemical Performance and Morphology Evolution of Silicon Nanowire Based Lithium-Ion Battery Anodes. *J. Power Sources* 2017, 359, 601.
- (4) Le, P. M. L.; Vo, T. D.; Pan, H.; Jin, Y.; He, Y.; Cao, X.; Nguyen, H. V.; Engelhard, M. H.; Wang, C.; Xiao, J.; Zhang, J. G. Excellent Cycling Stability of Sodium Anode Enabled by a Stable Solid Electrolyte Interphase Formed in Ether-Based Electrolytes. *Adv. Funct. Mater.* 2020, 30, 2001151.
- (5) Eshetu, G. G.; Diemant, T.; Hekmatfar, M.; Grugeon, S.; Behm, R. J.; Laruelle, S.; Armand, M.; Passerini, S. Impact of the Electrolyte Salt Anion on the Solid Electrolyte Interphase Formation in Sodium Ion Batteries. *Nano Energy* 2019, 55, 327–340.